Dual DNA-binding capability of Cdc13 coordinates with Ku to safeguard telomere integrity

Zhitong Feng, Jiangchuan Shen, Yuxi Li, Giovanni Gonzalez-Gutierrez, Quan Wang*, Hengyao Niu*

Department of Molecular and Cellular Biochemistry, Indiana University at Bloomington

Abstract

Telomeres protect chromosome ends from degradation and inappropriate DNA repair. In budding yeast, the telomeric protein Cdc13 binds G-rich overhangs to maintain telomere integrity. Here, we show that Cdc13 also weakly interacts with adjacent duplex DNA at the ss/dsDNA junction—a property essential for inhibiting Exo1- and Sgs1–Dna2–mediated resection. Mutation of a conserved residue (K504E) disrupts this junction recognition and impairs resection inhibition, RPA displacement, and cooperation with Ku. cdc13-K504E cells are hypersensitive to Exo1 overexpression and accumulate non-pigmented revertant colonies during chronic growth. These white colonies exhibit faster growth, altered telomere-proximal gene expression, upregulation of metabolic pathways, and increased 4N DNA content. Our findings identify a dual DNA-binding mode of Cdc13 that protects telomeres by blocking resection and regulating Ku positioning, and reveal a stress-induced adaptive state associated with telomere dysfunction.

Introduction

Telomeres are specialized nucleoprotein structures that cap the ends of linear chromosomes and are essential for preserving genome integrity. They prevent chromosome ends from being recognized as double-strand breaks (DSBs), thereby avoiding aberrant repair events such as end-to-end fusion, translocation, and genome instability[1-3]. In eukaryotes, telomeres typically consist of repetitive G-rich DNA ending in a 3′ single-stranded overhang, which in humans spans several kilobases of TTAGGG repeats, and in *Saccharomyces cerevisiae* consists of ~300 bp dsDNA and a 12–15 nt TG□_□ 3′ overhang[1,3,4].

Despite their protective role, telomeres pose a unique paradox: they must simultaneously suppress DNA damage responses while still permitting telomeric DNA ends processing, which is essential for telomere maturation[2,3]. This dilemma is most evident during S phase, when telomeric ends undergo maturation involving limited nucleolytic resection and telomerase catalyzed 3’ end extension[4,5]. In budding yeast, crucially, the same nucleolytic resection machinery essential for telomere maturation – which generates the 3' overhang required for telomerase action – is also central to homologous recombination (HR) repair of double-strand breaks (DSBs)[6-9]. This DNA end resection is primarily executed by three conserved pathways: the MRX complex (Mre11-Rad50-Xrs2) with Sae2, the exonuclease Exo1, and the helicase-

nuclease duo Sgs1–Dna2[6,7,10-12]. While limited resection is indispensable for telomere maintenance, uncontrolled or aberrant resection poses a significant threat to telomere integrity[4,10,13]. This inherent conflict underscores why restraining resection is critical for telomere protection. To resolve this paradox, cells have evolved “telomere capping” complexes (e.g., shelterin in mammals)[2] that preserve the telomere’s integrity while regulating resection/repair enzymes' access to chromosomal ends[2,3,9].

In budding yeast, telomere capping involves three major modules: the Ku70/80 heterodimer, the Rap1–Rif1/2 complex, and the CST complex (Cdc13–Stn1–Ten1)[4,14]. Rap1 and its associated factors, Rif1/2, occupy the telomeric dsDNA region, regulate telomere length and subtelomeric silencing[15,16]. The Ku heterodimer also encircles telomeric dsDNA and protects against 5′ exonucleolytic degradation[17-21], although Ku is more widely found at the ss/dsDNA junction of double-strand breaks (DSBs) to promote non-homologous end joining (NHEJ)[22,23]. Central to end protection is the CST complex, whose core component Cdc13 binds the 3′ overhang with high affinity. Structurally, Cdc13 contains four oligonucleotide/oligosaccharide-binding folds (OB-folds) and a telomerase recruitment domain (RD)[24,25]. The N-terminal OB1 mediates homodimerization with auxiliary ssDNA-binding capacity, while OB3 harbors the core telomeric G-strand recognition activity (Fig. S1A) [26,27]. This ssDNA engagement is essential for yeast viability, shielding telomeric termini from degradation while facilitating telomerase recruitment and C-strand fill-in for telomere maturation [28,29].

Notably, the CST complex demonstrates significant evolutionary conservation and functional divergence. In humans, CST plays essential roles in telomere replication and maturation, thereby contributing to telomere stability, and also participates in genome-wide replication regulation.[30-32]. Defects in CST components are associated with several human disorders, including Coats plus syndrome and dyskeratosis congenita, characterized by telomere dysfunction, genome instability, and cancer predisposition[33-37]. Aberrant CST expression is increasingly linked to tumorigenesis, underscoring the importance of understanding its molecular mechanisms.

Despite these advances, a fundamental question persists in the yeast model How does Ku—a core NHEJ factor dedicated to end joining[17] —persistently localize to telomeres without catalyzing catastrophic end-to-end fusions? This perplexing behavior implies specialized mechanisms actively suppress Ku's repair activity at chromosome ends. Yet, the mechanisms silencing this potentially deleterious repair activity at chromosome ends remain poorly understood.

Here, we uncover a novel DNA-recognition interface of Cdc13 that enables it to bind not only telomeric ssDNA but also display a preference for the ss/dsDNA junctions[38]. We show that this dual binding capability is essential for Cdc13 to suppress both Exo1- and Sgs1–Dna2-mediated resection and to facilitate Ku repositioning from ss/dsDNA junctions. Unlike *cdc13*Δ, mutations that impair this interaction don’t cause lethality, nor telomere shortening. However, it sensitizes the cells to resection stress in a manner that is synergistic with Ku mutations. Interestingly, the

junction binding mutant of Cdc13 led to the arise of colonies with greater fitness during the stationary phase and the fitness gain can be carried to vegetative growth as well. FACS analysis suggested these colonies have faster cycling with an increase in the S/G2 population, and G2 synchronization analysis revealed a subset of 4N population that may suggest cell cycle dynamics or diploid formation. Overall, our findings suggest Cdc13 may modulate Ku activity via its junction recognition to both synergize with Ku in counteracting end resection stress at telomeres and likely suppress Ku mediated end-joining at the same time. The loss of this junction recognition, while not essential for telomere maintenance during vegetative growth, may promote adaptive changes of cells in the stationary phase. These insights bridge fundamental telomere biology with mechanisms underlying age-related disorders and cancer.

Cdc13 interacts with ss/dsDNA junctions with enhanced affinity for telomeric 3′ overhangs

Cdc13 protects telomeric DNA largely through its DNA binding. To investigate its role in telomere protection, we first examined the substrate specificity of Cdc13 in telomeric DNA binding. To do so, recombinant full-length Cdc13 protein with an N-terminal SUMO tag was expressed in *E. coli* and purified to near homogeneity (Fig. S1B). After SUMO tag removal, mass photometry showed that Cdc13 revealed a major monomeric population and a minor dimeric form (Fig. S1C), consistent with previous biophysical studies[27].

To characterize the DNA-binding activity and specificity of the purified Cdc13 protein, we designed a panel of DNA substrates with identical duplex regions but varying 3′ overhangs to mimic different telomeric contexts: Tel14 (14-nt TG□-□ overhang) reflecting the physiological range of mature yeast telomeres[4]; Tel22 representing an extended overhang optimal for engaging two Cdc13 molecules, based on prior studies showing that each Cdc13 binds a minimum of ~11 nt[39,40]; and Tel7 (truncated 7-nt TG□-□ overhang) serving as a minimal-length control. In addition, a non-telomeric poly-dT overhang of 22 nt (T22) was included as a sequence specificity control. Electrophoretic mobility shift assays (EMSAs) under physiological salt conditions (150 mM KCl) revealed that Cdc13 binds Tel14 and Tel22 with high affinity, exhibiting distinct, cooperative banding patterns and apparent Kd values of ~5 nM and <2.5 nM, respectively, indicative of tight interactions (Fig. 1A). In contrast, the non-telomeric poly-dT substrate T22 showed much weaker binding (Kd ~80–100 nM), underscoring the sequence specificity of Cdc13 for telomeric G-rich ssDNA (Fig. 1A). Surprisingly, we also observed weak but detectable binding with Tel7 (apparent Kd ~40 nM) (Fig. 1A), in stark contrast to its negligible binding to 7-nt ssDNA (ssTel7, Fig. S1D). This disparity aligns with prior reports that Cdc13 requires ≥11 nt for stable ssDNA binding[39,40] and indicates that the duplex junction may compensate for suboptimal overhang length by providing additional contacts.

To confirm this, we conducted a competition assay of two substrates: ssDNA of telomeric sequences (ssTel22) and 3' overhang of telomeric sequences (Tel22). When both substrates were present in EMSA, Cdc13 strongly favored Tel22 over ssTel22 (Fig. 1B), suggesting that junction structure contributes to overall affinity. We next directly assessed Cdc13 binding to a blunt-ended

26-bp duplex substrate (ds26) and observed that Cdc13 binds ds25 with an apparent Kd of ~300 nM. This interaction is specific and was not observed with RPA (Fig. 1C) —the universal ssDNA binding protein in eukaryotes[41], confirming Cdc13's capacity to engage double-stranded DNA. In summary, these results demonstrate that Cdc13 binds telomeric 3′ overhangs with sequence and length dependence, and that duplex recognition at the ss/dsDNA junction enhances its binding affinity. We surmise that this dual engagement mode distinguishes Cdc13 from RPA and may underlie its specific function in telomere protection.

Conserved K504 is essential for telomeric ss/dsDNA junction recognition by Cdc13

To explore the structural basis of duplex recognition by Cdc13, we first examined available structural information of its DNA-binding domain. Analysis of the *K. lactis* Cdc13 OB2-OB4 crystal structure (PDB: 6LBR)[42] revealed an auxiliary α-helix near the OB3 N-terminus. This helix positions its side chains toward the phosphate backbone of 5'-terminal nucleotides A1-A5 (figu. 2A(i)). Notably, a lysine residue (K521) in this helix is positioned 3.3 Å from the DNA backbone, suggesting possible electrostatic interactions (Fig. 2A(i)). Sequence alignment confirmed that this lysine is evolutionarily conserved among fungal Cdc13 homologs (Fig. S9), and the spatial arrangement is preserved in the *S. cerevisiae* Cdc13 OB3 structure (PDB: 1KF1[43], Fig. 2A(ii)). Based on the alignment, we hypothesized that this lysine—K504 in *S. cerevisiae*—may play a role in recognizing the ss/dsDNA junction upon binding to telomeric 3′ overhang.

To test this hypothesis, we generated and purified the K504E point mutant of full-length Cdc13 (Fig. S2A), which displayed a similar monomer/dimer distribution as the wild-type protein in mass photometry (Fig. S2B). EMSAs using either the duplex DNA substrate ds26 or the minimal telomeric ss/dsDNA junction mimic Tel7 showed that Cdc13-K504E had markedly reduced binding compared to wild-type (Fig. 2B, 2C), consistent with impaired junction engagement. In contrast, binding to longer telomeric overhangs (Tel14 and Tel22) (Fig. 2D, 2E), as well as fully single-stranded ssTel22 substrate (Fig. S2C), was largely retained, suggesting that the mutation selectively disrupts duplex or junction recognition while preserving ssDNA binding.

Telomeric ss/dsDNA junction recognition by Cdc13

To further examine the binding and protection of telomeric ss/dsDNA junctions by Cdc13, we performed DNase I footprinting using L-Tel22, a substrate consisting of a longer duplex region (58 bp) with a 22-nt 3′ telomeric overhang. Cdc13 protected approximately 3 bp of duplex DNA immediately at the ss/dsDNA junction (Fig. 2F, S2D), consistent with prior reports [44]. Notably, the OB_{234} fragment of the *S. cerevisiae* Cdc13 (Fig. S1) also retained duplex protection, supporting these domains, but not OB1, mediate junction recognition. In contrast, the Cdc13-K504E mutant completely lost the duplex protection, indicating a failure to stably engage the duplex region at the junction. These findings affirm the critical role of K504 in Cdc13's unique ability to recognize telomeric ss/dsDNA junctions[38], while ssDNA binding per se remains largely intact.

Cdc13 suppresses Exo1-catalyzed DNA end resection by junction protection

As a crucial telomere end-protection factor, Cdc13 safeguards mature telomeres against degradation by the Exo1 and Sgs1-Dna2 resection machinery[13]. We previously reported that duplex recognition is essential for Exo1 activation (REF). To determine how Cdc13's junction binding contributes to this protection, we first assessed Cdc13's impact on Exo1 nuclease activity using 3'-overhang substrates of various lengths and sequences. On Tel22 and Tel14 substrates, addition of 20 nM Cdc13 significantly inhibited the initial cleavage by Exo1 (3-fold inhibition, $p < 0.0001$, n = 3) (Fig. 3A, S3A(i)). The effect was sequence specific as Cdc13 had no significant effect on Exo1 cleavage of T22 ($p = 0.15$, n = 3) (Fig. S3A(ii)). In addition, no direct interaction was detected between Cdc13 and Exo1 by pull-down (Fig. S3B), suggesting that Cdc13 exerts its function through DNA binding alone. Interestingly, RPA, which binds ssDNA but lacks junction specificity, only modestly affected Exo1 activity on tested substrates (<20% inhibition), supporting that the strong Cdc13 inhibitory effect on Exo1 is not only from its ssDNA binding (Fig. 3A, S3A(i)). The K504E mutant, which is defective in duplex recognition, is largely defective in Exo1 inhibition on both Tel22 and Tel14 substrates (Fig. 3B, S3C). Hence, Cdc13's junction binding may competitively exclude Exo1 from its substrate DNA.

Cdc13 suppresses Sgs1-Dna2 catalyzed DNA end resection by junction interaction.

Beyond Exo1-mediated resection, Sgs1 helicase and Dna2 nuclease constitute another key machinery for DNA end processing, where RPA serves as an essential component[45,46]. To understand how Cdc13 regulates this Sgs1-Dna2-RPA resection pathway, we first investigated the impact of Cdc13 on the activities of each component in this pathway. Using Tel7, Tel14, and Tel22 as substrates, we found that Sgs1 alone unwound the telomeric overhangs with a preference for a longer 3’ overhang (Fig. 4A, S4A). The addition of RPA enhanced this unwinding, most significant on the Tel7 substrate (Fig. 4A, S4A), which is consistent with a previous report[47]. On the other hand, the full-length Cdc13 (20 nM) mildly inhibited Sgs1-mediated unwinding, showing ~25% relative reduction on Tel22 and Tel14 (Fig. 4B, S4B), which was lost with the K504E mutant (≤5% reduction) (Fig. 4B, S4B).

Dna2 is a ssDNA endonuclease. We first asked how Cdc13 affects Dna2-catalyzed 5’ C-strand digestion which occurs during DNA end resection. To do this, we also compared Dna2 resection inhibition by RPA and Cdc13 on two different 5’ overhang substrates, a 5’-C-rich overhang (5’-C22) representing the strand subjected to resection at telomeric DNA end and a 5’-G-rich overhang (5’-Tel22) control. While Cdc13 efficiently inhibited Dna2 activity on 5’-Tel22 (Fig. S4C(ii)), it had little effect on 5’-C22 (a 5’-C-rich overhang) (Fig. S4C (iii)). In addition to 5’ resection, we also compared RPA and Cdc13 in the protection of 3’ overhang from Dna2 digestion. In this case, both RPA and Cdc13 protected Tel22 (a 3’-G-rich overhang) from Dna2 digestion (Fig. S4C(i)). These data establish that Cdc13's suppression of Dna2 requires G-rich sequences but is independent of DNA end polarity (3' vs 5'). Also, Cdc13 can substitute for RPA in the protection of 3’ telomeric ssDNA.

Given RPA's essential role in the Sgs1-Dna2 pathway and the opposing effects of Cdc13 versus RPA on Sgs1 and Dna2 activities, we performed competition EMSAs to assess their relative telomeric DNA binding. Under physiological salt (150 mM KCl), Cdc13 effectively outcompeted RPA for Tel22/Tel14 binding even when co-incubated with excess RPA at the same concentration (20 nM) (Fig. 4C, S4D). This dominance aligns with Cdc13's superior binding affinity for telomeric DNA.

Collectively, these findings demonstrate that Cdc13-mediated suppression of the Sgs1-Dna2 pathway operates largely through competitive displacement of RPA from G-rich strands, following the initiation of end reaction. Cdc13, on the other hand, efficiently protects the nascent G-strand from Dna2-catalyzed nucleolytic degradation. This selective protection strategy is physiologically critical for maintaining telomeric G-overhang integrity during telomere end-processing events.

Cdc13 modulates Ku binding at telomeric ss/dsDNA junctions and cooperates to suppress resection by Sgs1-Dna2.

In yeast, Ku70/80 complex is another key telomere factor reported to occupy ss/ds junction as well and known to suppress Exo1[48-50]. To understand how Cdc13 acts with Ku70/80 in the protection of telomeric DNA, we first asked how Cdc13 and Ku—both ss/dsDNA junction binders—resolve spatial conflict. Although yeast Ku prefers ss/ds junction[48], high-resolution ChIP at telomeres showed that Ku localizes at the telomere–subtelomere junction and at distal internal telomeric sequences (ITSs) far from chromosome ends[20]. We hypothesized that Cdc13 may alter Ku's binding configuration to permit co-occupancy. DNase I footprinting on L-Tel22 under sequential loading conditions showed that Ku alone protected ~15 bp near the junction (Fig. 5A, S5A), which is similar to a previous published result[48]. Adding Cdc13 to Ku-bound DNA broadened but weakened general protection (Fig. 5A, S5A). This redistribution indicates Cdc13 remodels pre-bound Ku complexes, displacing them from the ss/dsDNA junction—an effect abolished by K504E.

To explore the mechanism underlying this effect, we used a 2-aminopurine (2AP) base-flipping assay. 2AP, placed at the first base pair of the duplex region, fluoresces weakly when stacked but strongly upon base flipping, serving as a reporter of local distortion[51,52]. Cdc13 markedly increased 2AP fluorescence ($p < 0.0001$, n = 3), indicating local base flipping (Fig. 5B(i)). The fluorescence remained high with both Cdc13 and Ku ($p < 0.01$, n = 3), but not with Ku alone ($p > 0.1$, n = 3), confirming that the conformational change was Cdc13-driven. Cdc13-K504E and RPA had no significant effect ($p > 0.1$ and $p = 0.039$, respectively, n=3) (Fig. 5B(ii)).

Functionally, this remodeling enables cooperative resection suppression. Reconstitution of the Sgs1-Dna2-RPA pathway showed that Ku and Cdc13 individually reduced resection (Fig. 5C), while their combination produced additive inhibition. EMSAs under sequential loading conditions—where Ku was pre-bound to Tel22 before Cdc13 addition[53]—revealed a stable super-shifted complex (Fig. S5B). This ordered assembly confirms that Cdc13 remodels pre-

loaded Ku rather than blocking its binding, enabling spatial co-occupancy. This synergy was abolished by the Cdc13-K504E mutant, which neither suppressed resection nor enhanced Ku function.

Together, these results show that both Cdc13 and Ku coordinate junction occupancy and protect telomere against Sgs1-Dna2 end resection. Cdc13 induces base flipping at the junction-proximal position. This flipping activity likely facilitates Ku repositioning and is dependent on the integrity of Cdc13's junction-binding domain.

cdc13-K504E and Ku mutants lead to resection-sensitive growth defects

Having established that Cdc13-K504E impairs junction recognition and resection inhibition in vitro, we next asked whether these defects translate to physiological consequences in vivo. We therefore evaluated the growth phenotypes of *cdc13*-K504E and/or *ku80Δ* cells under conditions that challenge telomere integrity. Unlike the *cdc13-1*[54,55], *cdc13*-K504E strains grew comparably to wild type at both 30°C and 37°C (Fig. S6A, S6B). Although *ku80Δ*, as reported[56], showed temperature sensitive at 37□, *cdc13*-K504E *ku80Δ* is still viable with a temperature sensitive phenotype similarly to *ku80Δ* (Fig. S6A, S6B), indicating that the junction-binding defect does not aggravate this temperature sensitivity. We then measured telomere length by Southern blot. As reported for Ku's role in telomere length maintenance[17,57], *ku80Δ* shortened telomeres irrespective of Cdc13 status, whereas *cdc13*-K504E maintained normal telomere length (Fig. S6C), suggesting that junction recognition is dispensable for telomerase-mediated elongation. To further challenge telomeric DNA protection, we overexpressed Exo1 using a galactose inducible system. Overexpression of Exo1 resulted in approximately a 10-fold reduction in viability in *cdc13*-K504E strains (Fig. 6A). Deletion of Ku80 also showed a 10-fold reduction in viability (Fig. 6A); notably, the *cdc13*-K504E *ku80Δ* double mutant cells showed a synthetic growth defect upon Exo1 overexpression, with viability reduced by over 100-fold compared to the wild type (Fig. 6A), indicating that Cdc13 and Ku cooperatively suppress excessive resection.

Cdc13-K504E mutation generates adaptive *ADE2* revertants during prolonged stationary phase

To assess the long-term consequences of impaired telomere capping, we subjected WT and cdc13-K504E cultures to prolonged stationary phase (15 days in YPD without dilution). We first evaluated cellular resilience by plating 200 cells per replicate after chronic stress exposure. Surprisingly, both strains exhibited comparable colony-forming efficiency after 15 days (Fig. S6D), indicating no gross defect in recovery capacity under telomere stress.

Unexpectedly, during this analysis, however, we observed a striking phenomenon: cdc13-K504E plates showed progressive accumulation of white, non-pigmented colonies (Fig. 6B), whereas WT controls remained predominantly red. Quantitative analysis revealed that white colonies increased progressively with extended incubation, reaching approximately 35% by day 9 and 45%

by day 15, whereas wild-type controls remained largely red, with white colonies comprising no more than 18% of the population under the same conditions (Fig. 6C).

In the yeast strain background used in this study (W303), colonies appear red due to the *ade2-1* nonsense mutation, which disrupts adenine biosynthesis and leads to pigment accumulation[58,59]. Restoration of *ADE2* function reverts colony color to white. To elucidate the genetic basis of this phenotypic switch, we sequenced the *ADE2* locus from eight independent *cdc13-K504E* white colonies. All eight harbored reversion mutations restoring the *ADE2* open reading frame (Fig. S6E), explaining their non-pigmented phenotype. White colonies (both WT and *cdc13-K504E*-derived) grew faster and to higher densities than red ones (Fig. S6F), consistent with a fitness advantage.

Whole-genome sequencing (WGS) of wild-type red (WT-red), *cdc13*-K504E red (K504E-red), and *cdc13*-K504E-derived white colonies (K504E-white) revealed comparable numbers and spectra of SNPs across samples (Fig. S6G), indicating that *ADE2* reversions represent adaptive rather than generalized mutagenesis.

Taken together, the progressive emergence of *ADE2+* revertants suggests that *cdc13-K504E* cells face prolonged telomere stress, and only those acquiring compensatory mutations (e.g., *ADE2* restoration) outcompete their progenitors.

Altered cell cycle dynamics and genome organization in cdc13-K504E white cells

Given their growth advantage and larger colony size, we examined whether changes in cell cycle distribution or ploidy contributed to the phenotype. To test this, we compared DNA content distributions across strains using flow cytometry. Fluorescence-activated cell sorting (FACS) of asynchronous cultures revealed that all four strains—WT-red, WT-white, K504E-red, and K504E-white—exhibited typical 1N and 2N peaks, but K504E-white cells showed marked S/G2 enrichment (Fig. S7A, S7B), suggesting faster cell cycles.

To determine whether this accelerated progression compromised genome integrity surveillance, we challenged cells with nocodazole–a microtubule-depolymerizing agent that arrests cells in G2/M phase and triggers the spindle assembly checkpoint (SAC). Following synchronization, K504E-white cultures accumulated a prominent 4N DNA population (5.0% ± 0.4%; Fig. 7C), indicative of SAC bypass or tetraploidization. This phenotype was absent in controls (≤2.2% 4N cells; Fig. 6D, S7C) and occurred without altering the 2N fraction (stable at ~80%; Fig. 6E, S7C).

These coordinated defects—accelerated cycling under basal conditions and failure to maintain checkpoint arrest under stress—demonstrate that telomere-driven adaptive evolution trades genome stability for proliferative fitness.

Transcriptomic reprogramming associated with the white colony state

To uncover the molecular basis of adaptation in the *cdc13*-K504E background, we compared the transcriptomes of wild-type red (WT-red), *cdc13*-K504E red (K504E-red), and *cdc13*-K504E

white (K504E-white) colonies by RNA sequencing. Principal component analysis showed clear segregation among these groups (Fig. S8A), confirming distinct transcriptional states. This analysis revealed a broad upregulation of metabolic genes in K504E-white colonies, encompassing critical pathways in adenine (e.g., *ADE2*, *ADE17*) and thiamine (e.g., *THI20*, *THI21*) biosynthesis (Fig. 7A, B). Genes showing significant transcription difference were further validated by RT–qPCR of key targets (Fig. S8C). This metabolic rewiring likely underlies the observed loss of red pigmentation and accelerated growth in these adaptants (Fig. S6E, S6F). Furthermore, Gene Ontology analysis indicated a coordinated shift in organelle-related processes (Fig. S8D, E), suggesting that the adaptive white state involves comprehensive reprogramming of cellular metabolism and architecture.

Comparisons of differentially expressed genes revealed 975 genes commonly affected by the K504E mutation, while 270 genes differed between red and white colonies, confirming progressive transcriptomic divergence (Fig. S8B). Notably, none of the differentially expressed genes—including *THI4* or *FRM2*—nor their flanking regions harbored detectable mutations in our whole-genome sequencing data, indicating their altered expression arises from transcriptional regulation rather than local genetic changes.

This transcriptional rewiring—uncoupled from genetic changes but tightly linked to the adaptive white state—completes a paradigm wherein telomere dysfunction drives genome evolution through both genetic (e.g., *ADE2* reversion) and epigenetic adaptations.

Discussion

Our study characterized a dual DNA-binding activity of the yeast telomeric protein Cdc13 that underlies its ability to inhibit nucleolytic degradation and inappropriate DNA repair. We found that in addition to its established high-affinity binding to the single-stranded telomeric 3′ overhang, Cdc13 also interacts with the adjacent duplex DNA at the ss/dsDNA junction via a conserved lysine residue (K504). This junction engagement is critical for suppressing Exo1- and Sgs1–Dna2-mediated resection and safeguarding chromosome ends.

Despite this defect, cdc13-K504E mutants do not exhibit immediate telomere shortening. This apparent resilience likely reflects functional buffering by other telomere-associated factors such as Rap1-Rif1/2 and the Ku complex, which also help maintain telomere structure and delay overt genome instability[4]. The delayed emergence of phenotypes suggests that junction-binding may contribute to long-term end protection, particularly under stress.

Although buffered in early passages, cdc13-K504E mutants ultimately exhibit profound cellular changes under during prolonged stationary phase. White colonies derived from long-term culture show distinct transcriptomic reprogramming, with strong upregulation of thiamine and adenine biosynthetic pathways. Flow cytometry further revealed an enrichment of cells in S/G2 phases and accumulation of a 4N DNA content population following nocodazole treatment, consistent with altered cell cycle dynamics or diploid formation. Whole-genome sequencing showed no

mutations near key upregulated genes such as THI4 or FRM2, suggesting that the expression changes reflect regulatory adaptation rather than local mutations.

Biochemically, junction binding by Cdc13 repositions Ku localization at chromosome ends. Our footprinting and base-flipping assays suggest that Cdc13 reshapes duplex DNA near the junction, releases Ku complex from ss/dsDNA and promotes its diffusion along duplex DNA. This spatial reorganization—encompassing Ku displacement, RPA exclusion, and resection blockade—collectively safeguards telomere integrity (Fig 7C). Specifically, this reorganization achieves two critical outcomes: (i) synergistic enhancement of resection inhibition, and (ii) displacement of Ku from the ss/dsDNA junction. This displacement of Ku, while enhancing resection protection, may also limit its capacity to catalyze NHEJ, thereby safeguarding telomere integrity by blocking both degradation and inappropriate repair.

This mechanism highlights a conserved protective strategy centered on ss/dsDNA junction recognition. However, its implementation differs between organisms. In budding yeast, which lacks a shelterin complex, the CST component Cdc13 acts as a multi-functional hub, directly binding the ssDNA overhang, engaging the junction, inhibiting resection, and modulating Ku positioning. In contrast, in mammals, junction recognition and the associated protection against resection are primarily executed by POT1 within the shelterin complex[2,31,60,61]. The functional analogy between Cdc13's junction binding and POT1's activity underscores the evolutionary conservation of junction-specific protective strategies, even as the division of labor among telomeric complexes has diverged. Critically, the maintenance of telomeric DNA-end architecture, particularly the integrity of the ss/ds junction, emerges as a fundamental requirement for genome stability across species. Given that the human CST complex plays indispensable roles in orchestrating telomeric DNA replication and ensuring the faithful maintenance of this end structure [35],—represent a direct compromise of this essential architectural safeguard[34]. Our detailed mechanistic dissection of how Cdc13 safeguards the junction to prevent degradation and constrain aberrant repair in yeast therefore provides a foundational framework for understanding how disruption of telomere-end integrity, whether during replication or end-protection, underlies the genomic instability characteristic of these human diseases.

Materials and Methods

Yeast Strains. Yeast strains used in this study are derivatives of HKY3415-11 (*MATa SRS2-TAP-TRP1, leu2-3, 112 his3-11, 15 ade2-1, ura3-1, trp1-1, can1-100, RAD5+*) (A kind gift from Dr. Hannah Klein, NYU). All strains are listed in Supplementary Table S2.

Yeast Growth Assays. Yeast strains (Table S2) were cultured in YPD medium (1% yeast extract, 2% peptone, 2% dextrose) at 30°C with shaking. Strains were maintained on YPD or -LEU plates as required.

For spot assays, overnight saturated yeast cultures were harvested and adjusted to an OD600 of 1. Cells were then serially diluted 10-fold and spotted onto appropriate plates. The plates were air-dried and incubated at 30°C.

For growth curve analysis, overnight cultures were diluted to OD_{600} = 0.2 and grown to the exponential phase. Exponentially growing cells were further diluted to OD_{600} = 0.2 in fresh medium and seeded into 96-well plates. OD_{600} was recorded every 30 minutes at 30□ using a plate reader.

DNA Substrates Preparation. All oligonucleotides were purchased from IDT, with sequences listed in Supplementary Table S1. For 5′-end labeling, oligonucleotides were radiolabeled with [γ-^{32}P] ATP using T4 Polynucleotide Kinase (New England Biolabs). For 3′-end labeling, oligonucleotides were labeled with Cy5-dUTP or Cy3-dUTP using terminal transferase (New England Biolabs). Excess ATP/dUTP nucleotides were removed using Bio-Spin 6 columns (Bio-Rad) before annealing complementary oligonucleotides in NEB Buffer 3.1 (50 mM Tris-HCl, pH 7.9, 100 mM NaCl, 10 mM $MgCl_2$, and 100 µg/mL BSA) following a standard thermal cycler protocol. Notably, the ssTel7 substrate was not subjected to Bio-Spin 6 cleanup due to its short length.

Cdc13, Cdc13-K504E and Cdc13-OB_{234} Expression and Purification. The pET28a–His-SUMO–Cdc13-Flag/pET28a–His-SUMO–Cdc13-K504E-Flag/ pET28a–His-SUMO–Cdc13-OB_{234}-Flag (341-924) construct was transformed into *E. coli* BL21 (DE3) codon plus cells. Transformed cells were plated on Luria-Bertani (LB) agar containing 50 µg/mL kanamycin and incubated overnight at 37°C. A single colony was picked and inoculated into 2 L of LB liquid medium supplemented with 100 µg/mL kanamycin and grown statically at 37°C overnight. The culture was then shaken at 150 rpm until the optical density at 600 nm (OD_{600}) reached 0.6–0.8. Protein expression was induced by adding isopropyl-β-D-1-thiogalactopyranoside (IPTG) to a final concentration of 0.5 mM, followed by incubation at 18°C overnight. Cells were harvested by centrifugation at 5,000g for 20 minutes, and the resulting cell pellets were stored at −80°C.

For protein purification, cell pellets from 12 L of culture were thawed and resuspended in 250 mL of buffer (40 mM KH_2PO_4, 500 mM KCl, 10% glycerol, 0.01% NP-40, 1 mM TCEP, pH 7.4) supplemented with 1 mM PMSF and a protease inhibitor cocktail (5 µg/mL each of aprotinin, chymostatin, leupeptin, and pepstatin A). Cells were lysed on ice using sonication for 10 minutes, and the lysate was clarified by centrifugation at 20,000g for 20 minutes. The supernatant was applied to a 2 mL Ni-NTA resin column (GE Healthcare) equilibrated with K buffer (40 mM KH_2PO_4, 500 mM KCl, 0.1% NP-40, 1 mM TCEP, and 15 mM imidazole). The column was washed twice with 20 mL of K buffer (40 mM KH_2PO_4, 500 mM KCl, 0.01% NP-40, 1 mM TCEP, and 15 mM imidazole), and the protein was eluted with 15 mL of K buffer containing 200 mM imidazole. The eluate was diluted 1:1 with K buffer (0.01% NP-40, 1 mM TCEP) and incubated overnight at 4°C with 0.5 mL anti-Flag beads and 5 µg Upl1 protease for SUMO cleavage. The Flag beads were washed twice with 10 mL K buffer (40 mM KH_2PO_4, 500 mM

KCl, 0.1% NP-40, and 1 mM TCEP) and then with 20 mL K buffer (40 mM KH_2PO_4, 500 mM KCl, 0.01% NP-40, 1 mM TCEP). Bound protein was eluted with 5 mL of K buffer containing 200 µg/mL FLAG peptide and concentrated to 1 mL using an Amicon Ultra centrifugal filter (30 kDa cutoff, Millipore). The concentrated protein was further purified by size-exclusion chromatography using a Superdex 200 Increase 10/300 GL column (GE Healthcare). Fractions containing the target protein were pooled, concentrated to 0.5–1 mg/mL, and aliquoted in 10 µL volumes. The aliquots were flash-frozen in liquid nitrogen and stored at −80°C for future use.

Exo1 Expression and Purification. The pET21a-Exo1 plasmid was transformed into Rosetta (DE3) pLys cells. An overnight culture was diluted 1:50 into 12 liters of Luria-Bertani (LB) medium containing 100 µg/mL ampicillin. Protein expression was induced with 0.5 mM isopropyl 1-thio-β-d-galactopyranoside (IPTG) when the culture reached an OD_{600} of 0.6–0.8, followed by incubation overnight at 16 °C. Cells were harvested by centrifugation, yielding approximately 30 g of cell pellet, which was stored at -80 °C for future use.

All purification steps were conducted at 4 °C. The cell pellet was resuspended in 150 mL of lysis buffer (pH 7.4) containing 40 mM KH_2PO_4 and 150 mM KCl, 0.5 mM EDTA, 10% glycerol, 40 mM KH_2PO_4, 0.01% NP-40, 1 mM β-mercaptoethanol, and a cocktail of protease inhibitors. Cells were lysed by sonication, and the lysate was clarified by centrifugation at 20,000 × g for 20 minutes. The supernatant was then loaded onto a 5-mL sulfopropyl-sepharose column and washed with 50 mL of washing buffer (pH 7.4) containing 40 mM KH_2PO_4 and 150 mM KCl before Exo1 was eluted with 50 mL of elution buffer (pH 7.4) containing 40 mM KH_2PO_4 and 500 mM KCl.

The eluate was incubated with 400 µL of nickel-nitrilotriacetic acid resin for 1.5 hours, followed by washing the resin with 30 mL of wash buffer (pH 7.4) containing 40 mM KH_2PO_4, 500 mM KCl and 15 mM imidazole. Exo1 was eluted in three fractions of 0.4 mL each using a stepped imidazole gradient of 50, 100, and 200 mM. The purified Exo1 protein, which peaked in the fraction containing 200 mM imidazole, was aliquoted and stored at -80 °C for future experiments.

Ku Expression and Purification. The experimental procedure closely followed the method described by Krasner et al. (2015). The coding regions of YKU70 and YKU80 were cloned into the pESC-Ura vector, using the same plasmid constructs as in the referenced study. A FLAG tag was introduced at the C-terminus of Yku80 to facilitate detection and purification. Protein expression was carried out in the protease-deficient yeast strain BJ5464. Purification was performed using a two-step approach: DEAE-Sepharose chromatography followed by FLAG affinity purification, as detailed in Krasner et al. (2015).

RPA Expression and Purification. RPA was expressed and purified as described previously[47].

Dna2 Expression and Purification. Dna2 was expressed and purified as described previously[47].

Electrophoretic mobility shift assays. Electrophoretic mobility shift assays were performed in a 10 µL reaction system containing 20 mM Tris-HCl (pH 8.0), 2 mM $MgCl_2$, 150 mM KCl, 1 mM

DTT, 200 μg/mL BSA, 5 nM DNA substrate, and the indicated amounts of proteins. The samples were incubated at 30°C for 10 minutes. For each reaction, 2 μL of 6x loading dye (10 mM Tris-HCl (pH 8.0), 0.025% (w/v) orange G, 50% glycerol) was added. For the competition assay between RPA and Cdc13/Cdc13-K504E, RPA was added first and incubated at 30°C for 10 minutes, followed by the addition of Cdc13 or Cdc13-K504E and an additional incubation at 30°C for 10 minutes. In the competition assay between ssDNA and the 3' overhang, 5 nM of each substrate was pre-mixed, and Cdc13 was added, followed by a 10-minute incubation at 30°C. The samples were then fractionated on a 6% native polyacrylamide gel run in 0.5x TBE (Tris-borate-EDTA) buffer, followed by phosphor-imaging analysis.

Exo1 Resection Assays. Exo1 nuclease assays were performed in a 10 μL reaction system containing 5 nM DNA substrate. The DNA substrate was first incubated with the indicated amounts of ssDNA binding proteins in the reaction buffer (20 mM Tris-HCl pH 8.0, 2 mM $MgCl_2$, 150 mM KCl, 1 mM DTT, and 200 μg/mL BSA). The mixture was incubated at 30°C for 10 minutes before adding Exo1. The reaction was then incubated at 30°C for an additional 10 minutes. To terminate and deproteinize the reaction, 0.2% SDS and 0.5 mg/mL proteinase K were added, and the sample was incubated at 37°C for 5 minutes, followed by heat treatment at 95°C for 5 minutes in loading buffer (95% formamide, 0.025% (w/v) bromophenol blue, 0.025% (w/v) orange G, and 5 mM EDTA). The sample was then chilled on ice for 5 minutes and fractionated by 20% polyacrylamide denaturing gel electrophoresis in 0.5x TBE (Tris-borate-EDTA) buffer, followed by phosphor-imaging analysis.

Sgs1-Dna2 Resection Assays. Assays were conducted in a 10 μL reaction system containing 5 nM DNA substrate and the indicated amounts of DNA binding proteins, which were incubated at 30°C for 10 minutes the reaction buffer (20 mM Tris-HCl pH 8.0, 2 mM $MgCl_2$, 150 mM KCl, 1 mM ATP, 1 mM DTT, and 200 μg/mL BSA) before adding the enzyme mixture. The enzyme mixture was pre-mixed to achieve final concentrations of 5 nM Sgs1, 5 nM Dna2, and 20 nM RPA in the reaction. The reaction was then incubated at 30°C for 10 minutes. To stop and deproteinize the reaction, 0.2% SDS and 0.5 mg/mL proteinase K were added, and the sample was incubated at 37°C for 5 minutes, followed by heat treatment at 95°C for 5 minutes in loading buffer (95% formamide, 0.025% (w/v) bromophenol blue, 0.025% (w/v) orange G, and 5 mM EDTA). The sample was subsequently chilled on ice for 5 minutes and fractionated by 20% polyacrylamide denaturing gel electrophoresis in 0.5x TBE (Tris-borate-EDTA) buffer, followed by phosphor-imaging analysis.

DNase I Footprinting. The reaction (20 μL) was prepared in a buffer containing 10 mM Tris-HCl (pH 7.5), 2.5 mM $MgCl_2$, and 0.5 mM CaCl2. Ku was first incubated with the DNA substrate for 10 minutes at 30°C, followed by the addition of Cdc13 or its mutants, and incubated again at 30°C. DNase I (0.05 U) was then added, and the reaction was further incubated for 5 minutes at 25°C. The reaction was terminated by boiling in formamide loading dye, followed by analysis on 15% a denaturing TBE polyacrylamide gel.

In Vitro Competition Assay. Tel22 and Tel14 (5 nM each) were incubated with RPA (20 nM) in a reaction buffer containing 20 mM Tris-HCl (pH 8.0), 2 mM MgCl□, 150 mM KCl, 1 mM DTT, and 200 μg/mL BSA. RPA was first incubated at 30°C for 10 minutes, followed by the addition of Cdc13 at varying concentrations (2.5, 5, 10, 20, and 40 nM) and further incubation at 30°C for another 10 minutes. Correlation curves and quantifications, including the mean and standard deviation, were derived from three independent experiments. Solid and dashed lines in the correlation curves represent Cdc13 and RPA, respectively.

Telomere Southern Blot Southern Blot Analysis. Genomic DNA was extracted from Saccharomyces cerevisiae and digested overnight with XhoI. Digested DNA was separated on a 0.8% agarose gel and transferred onto a positively charged nylon membrane (Hybond-N+, Amersham) by capillary blotting in 10× SSC. DNA was UV crosslinked to the (120 mJ/cm^2).

A telomeric probe (5'-ACACCCACACCCACACCCACACCC-3') was labeled using the DIG High Prime DNA Labeling Kit (Roche). The probe was hybridized to the membrane in prewarmed hybridization buffer at 55°C overnight. The membrane was washed under stringent conditions and incubated with anti-DIG-AP antibodies (Roche). Signal detection was performed using chemiluminescent substrates, and images were acquired using an imaging system.

2-AP Fluorescent Assay. 2AP fluorescent samples were excited at 315 nm, and emission was detected at 370 nm with a Photon-counting spectrometer PC1 (ISS Inc). The reaction buffer contained 20 mM Tris-HCl (pH 8.0), 2 mM $MgCl_2$, 150 mM KCl, 1 mM DTT, and 200 μg/mL BSA. Experiments were performed under room temperature with Ku (80 nM) or/and Cdc13/Cdc13-K504E (80 nM)

Affinity pull-down assay. Exo1-His_6 (1.2 μg) and Cdc13-Flag (1.5 μg) were incubated in 50 μL binding buffer (K150, 1 mM DTT) at 4°C for 1.5 hours. After incubation, 10 μL of the reaction mixture was taken as the input sample. The reaction was then incubated with Flag-beads, followed by centrifugation at 10,000g for 5 minutes to collect the flow-through. Beads were washed three times with 0.8 ml wash buffer (K150, 1 mM DTT, 0.01% NP-40), and the wash fractions were collected. Bound proteins were eluted by incubating the beads in 1× SDS loading buffer at 95°C for 5 minutes.

Nocodazole-Induced G2/M Arrest and Flow Cytometry Analysis. Cells were cultured in YPD medium at 30°C with shaking until reaching a density of 0.5–1 × 10^7 cells/mL. Nocodazole was added to a final concentration of 15 μg/mL, followed by incubation at 30°C with agitation for 2–3 hours to arrest cells at G2/M phase. After treatment, cells were harvested and washed with water, then resuspended in 2% potassium acetate (KAc) and incubated on a shaker at 30°C for 1 hour. Cells were pelleted and fixed in 70% ethanol at room temperature for 2 hours or overnight at 4°C. Fixed cells were washed twice with 50 mM sodium citrate buffer, then incubated in sodium citrate containing 0.1 mg/mL RNase A at 37°C for at least 1 hour. Subsequently, cells were stained with 20 μg/mL propidium iodide (PI) in sodium citrate buffer with RNase A, protected from light, at room temperature for 1 hour or overnight at 4°C. Before

flow cytometry, cells were sonicated twice for 10 seconds at full power and diluted to approximately 5 × 10^5 cells/mL in sodium citrate buffer containing 5 μg/mL PI. Samples were then analyzed by flow cytometry to assess cell cycle distribution. Optional steps included microscopic verification of PI staining and proteinase K treatment (10 μL of 20 mg/mL at 55°C for 1 hour) if needed.

Mass photometry. Protein molecular weights were measured using a TwoMP mass photometer (Refeyn Ltd.) at room temperature. Samples were diluted to 20–50 nM in a buffer containing 40 mM KH□PO□, 500 mM KCl, 1 mM TCEP, pH 7.4 before measurement.

RNA extraction and sequencing. Total RNA was extracted from yeast cell samples by Novogene Co., Ltd. (Beijing, China) using their standard protocols. The extracted RNA was quality-checked and used to prepare mRNA libraries. RNA sequencing was performed on an Illumina NovaSeq X Plus platform with paired-end 150 bp reads (PE150), generating at least 6 Gb of raw data per sample. Sequencing quality was assessed with Q30 scores ≥ 85%. Raw data processing, including quality control, alignment to the Saccharomyces cerevisiae W303 reference genome (downloaded from the Saccharomyces Genome Database on June 28, 2025), and gene expression quantification, was performed using Novogene's internal pipelines.

RT-qPCR. RT-qPCR was performed on a Bio-Rad CFX system using SYBR Green detection chemistry. Actin was used as the reference gene, and relative expression levels were calculated using the 2^-ΔΔCq method, with WT as the calibrator. For each condition, two technical replicates were run; values are reported as mean ± SD. Melt-curve analysis confirmed single products and NTC/NRT controls showed no amplification.

RNA-seq data analysis. Normalized gene expression values were provided by Novogene. Raw and processed RNA-seq data have been deposited in the NCBI Gene Expression Omnibus (GEO) under accession GSE305992. Subsequent analyses, including calculation of gene distances to telomeres based on SGD genomic coordinates, and generation of heatmaps for genes within 20 kb of telomeres, were performed in-house using Python (pandas, seaborn).

Whole-genome sequencing (WGS). WGS was performed by Novogene. Raw sequencing reads and processed data have been deposited in the NCBI Sequence Read Archive (SRA) under BioProject accession PRJNA1308857.

Figure Legend

Figure 1. Cdc13 preferentially binds telomeric 3′ overhangs and ss/dsDNA junctions.

(A) EMSA showing binding of Cdc13 to 5′-labeled Tel7, Tel14, Tel22, and T22 substrates (5 nM each). All substrates contain an 18-bp duplex of random sequence followed by an 8-bp telomeric sequence but differ in the 3′ overhang: 7, 14, or 22 nt of telomeric G-rich DNA (Tel7–22) or 22 nt poly-T (T22).

(B) Competitive EMSA in which Cy5-labeled Tel22 competes with Cy3-labeled ssTel22 or excess ssDNA.

(C) EMSA comparing Cdc13 and RPA binding to a Cy5-labeled 26-bp blunt-end dsDNA (5 nM) under 150 mM KCl.

Figure 2. Lysine 504 is required for junction recognition by Cdc13.

(A) Structural comparison of *K. lactis* and *S. cerevisiae* Cdc13 DNA-binding domains. (i) Crystal structure of the *K. lactis* Cdc13DBD–Tel25 complex (PDB: 6LBR) showing Lys521 (red) positioned 3.3 Å from the DNA phosphate backbone near the 5′ end of the duplex. (ii) Structural alignment of *K. lactis* (cyan) and *S. cerevisiae* (green) Cdc13 DBDs, highlighting the conserved lysine K504 in S. cerevisiae. Structures were visualized and aligned using PyMOL.

(B-E) EMSA using 5′-labeled DNA substrates: blunt dsDNA (B), Tel7 (C), Tel14 (D), and Tel22 (E) at 5 nM. Cdc13 and Cdc13-K504E proteins were tested at increasing concentrations (5–80 nM) under 150 mM KCl. Quantification curves represent mean ± SD from three independent replicates.

(F) DNase I footprinting assay with L-Tel22 substrate (20 nM). The blunt end was labeled with ^{32}P (P32) and blocked by biotin–streptavidin. Cdc13, $Cdc13_{OB234}$, and Cdc13-K504E (80 nM) were preincubated before DNase I digestion. Protected regions are boxed; sizes indicated in nucleotide.

Figure 3. Cdc13 inhibits Exo1 via junction engagement.

(A-B) Exo1 resection assay using ^{32}P-labeled Tel22 substrate (5 nM). Cdc13, RPA or Cdc13-K504E (20 nM) was preincubated with DNA for 10 min, followed by addition of Exo1 (0.1, 0.2, or 0.5 nM). Quantification represents mean ± SD from three independent experiments.

Figure 4. Cdc13 suppresses Sgs1-Dna2 catalyzed DNA end resection

(A-B) Sgs1 unwinding assay with ^{32}P -labeled Tel22 (5 nM) and biotin–streptavidin blocked blunt ends. Cdc13, RPA or Cdc13-K504E (20 nM) was preincubated before addition of Sgs1 (5 or 20 nM). Quantification represents mean ± SD from three independent experiments.

(C) EMSA competition assay with ^{32}P -labeled Tel22 (5 nM). RPA binding was assessed in the presence of increasing concentrations of Cdc13 (2.5–40 nM). Quantification represents mean ± SD from three independent experiments.

Figure 5. Cdc13 cooperates with Ku to inhibit resection and remodels Ku localization at the telomeric ss/dsDNA junction.

(A) DNase I footprinting on ^{32}P-labeled L-Tel22 substrate (20 nM) with a blocked blunt end. Ku (80 nM), Cdc13-WT (80 nM), and Cdc13-K504E (80 nM) were added individually or in

combination. DNase I digestion (0.05 U) was performed at 25°C for 5 min after complex assembly. Molecular weights are indicated in nucleotides (nt lane).

(B) 2-Aminopurine (2AP) fluorescence assay using 2AP-labeled Tel22 substrate (20 nM). Cdc13, Cdc13-K504E, Ku, and RPA were added individually or in combination. Unpaired and fully paired DNA controls were included.

(C) Resection assay using ^{32}P-labeled Tel22 substrate (5 nM) with biotin–streptavidin blocked blunt ends. Sgs1 (5 or 20 nM), Dna2 (20 nM), and RPA (20 nM) were premixed and added with or without Ku (40 nM), Cdc13 (20 nM), or both. Quantification represents mean ± SD from three independent experiments.

Figure 6. *cdc13*-K504E generates adaptive *ADE2* revertants during prolonged stationary phase

(A) Growth assay of wild-type, *cdc13*-K504E, *ku80Δ*, and *cdc13*-K504E *ku80Δ* strains with Exo1 overexpression from plasmids. Cells were spotted onto selective raffinose or galactose plates at 30°C.

(B) Colony color reversion assay. WT and *cdc13*-K504E strains were cultured in liquid YPD for 3, 9, or 15 days, then plated on fresh YPD plates. Representative images are shown.

(C) Quantification of white colony frequency from 10 independent YPD plates on days 3, 9, and 15.

(D) Flow cytometry plots of asynchronous cultures treated with nocodazole for 2 h. 1N, 2N, and 4N peaks are indicated.

(E) Quantification of S/G2 and 4N populations across all strains after 2 h nocodazole treatment. Mean ± SD from three independent experiments is shown.

Figure 7. White cdc13-K504E colonies exhibit altered cell cycle progression and DNA content profiles.

(A-B) Volcano plot comparing K504E-red vs WT and K504E-white vs WT.

(C) Schematic model illustrating proposed Cdc13–Ku interaction at the telomeric ss/dsDNA junction.

Supplementary Figure S1. Expression, purification, and validation of Cdc13 protein.

(A) Domain schematics of *S. cerevisiae* Cdc13 and $Cdc13_{OB234}$.

(B) SDS-PAGE analysis of SUMO-tagged Cdc13 purified from *E. coli*. The SUMO tag was cleaved prior to downstream experiments.

(C) Mass photometry of purified Cdc13 showing peaks corresponding to monomeric and dimeric forms.

(D) EMSA showing binding of Cdc13 to 5′-labeled ssTel22 (5 nM).

Supplementary Figure S2. Biochemical characterization of Cdc13-K504E mutant.

(A) SDS-PAGE analysis of purified Cdc13-K504E mutant protein.

(B) Mass photometry of Cdc13-K504E showing peaks corresponding to the monomeric form.

(C) EMSA of Cdc13 and Cdc13-K504E binding to single-stranded Tel22. Quantification represents mean ± SD from three independent experiments.

(D) DNase I footprinting of L-Tel22 (20 nM) with ^{32}P labeling. The blunt end was blocked with biotin and streptavidin. Reverse labeling was used to generate distinct marker sizes.

Supplementary Figure S3. Control experiments for Exo1 resection analysis.

(A) Exo1 digestion assays (0.1, 0.2, or 0.5 nM) with or without prebound RPA (20 nM) or Cdc13 (20 nM) on ^{32}P-labeled Tel14 (i) and T22 (ii) substrates.

(B) Pull-down assay to assess interaction between Exo1 and Cdc13.

(C) Exo1 digestion assay (0.1, 0.2, or 0.5 nM) with prebound Cdc13 or Cdc13-K504E on ^{32}P-labeled Tel14 substrate.

Supplementary Figure S4. Control experiments for Sgs1-Dna2 resection analysis.

(A) Sgs1 unwinding assays (5 or 20 nM) on ^{32}P-labeled Tel14 (ii), and Tel7 (ii) substrates (5 nM) with biotin–streptavidin blocked blunt ends. Prebinding of RPA (20 nM) or Cdc13 (20 nM) was performed. Quantification represents mean ± SD from three independent experiments.

(B) Sgs1 unwinding assay under the same conditions as in (D) with Cdc13-K504E.

(C) Dna2 nuclease assays on 5′ C22 (i), Tel22 (ii), and 5′ Tel22 (iii) substrates.

(D) EMSA competition assay with ^{32}P -labeled Tel14 (5 nM). RPA binding was assessed in the presence of increasing concentrations of Cdc13 (2.5–40 nM). Quantification represents mean ± SD from three independent experiments.

Supplementary Figure S5. Ku footprint expansion.

(A) DNase I footprinting of with 5′ -^{32}P-labeled L-Tel22 (20 nM). The blunt end was blocked with biotin and streptavidin. This experiment complements the blunt-end labeling shown in Fig. 4B.

(B) EMSA of Ku and Cdc13 on Tel22 substrate. Supershifted complexes were assessed.

Supplementary Figure S6. Additional in vivo phenotypic analyses of cdc13-K504E.

(A) Growth curves of WT and *cdc13*-K504E ± *ku80Δ* strains at 30°C and 37°C.

(C) Temperature sensitivity assay of WT and *cdc13*-K504E ± *ku80Δ* strains on YPD plates. Plates were incubated at 30°C unless noted otherwise (25°C or 37°C).

(B) Southern blot analysis of telomere length in WT and *cdc13*-K504E ± *ku80Δ* strains.

(D) Colony formation assay of 15-day continuously cultured WT and cdc13-K504E cells. Cells were diluted and ~200 cells were plated on fresh YPD plates. The number of colonies formed per 100 plated cells was quantified. The y-axis represents colonies per 100 cells; the x-axis indicates strain. Quantification is shown as a grouped dot plot of WT and cdc13-K504E strains (n = 10 per group), with a horizontal line representing the mean.

(E) Sequencing of *ADE2* revertant colonies.

(F) Growth curves of red and white colonies from WT and cdc13-K504E strains in liquid YPD.

(G) Bar plots showing the distribution of SNP mutation types in whole-genome sequencing samples: WT-red (n = 1), K504E-red (n = 1), and K504E-white (n = 3). Each bar represents the fraction of SNPs of a given type in the corresponding sample.

Figure S7. Flow cytometry analysis of DNA content.

(A) Flow cytometry analysis of asynchronous cultures of WT-red, WT-white, K504E-red, and K504E-white strains. PI-Area (B610-A) vs Count histograms are shown.

(B) PI-Area vs PI-Width plots of asynchronous cultures. A single gate was used to select intact cells.

(C) PI-Area vs PI-Width plots of nocodazole-arrested cells. Three gates corresponding to 1N, 2N, and 4N populations are indicated with quantified percentages.

Figure S8. Principal component and overlap analysis of RNA-seq samples.

(A) Principal component analysis (PCA) of RNA-seq profiles from WT-red, K504E-red, and K504E-white strains.

(B) Venn diagram showing the overlap of differentially expressed genes among indicated comparisons.

(C) RT-qPCR analysis of selected genes in WT-red, K504E-red, and K504E-white colonies. Relative mRNA levels were measured using Actin as the reference gene and normalized to WT-red. Data are presented as mean ± SD from two technical replicates.

(D) Gene ontology (GO) enrichment analysis of K504E-red vs WT-red for Biological Process (BP), Cellular Component (CC), and Molecular Function (MF) categories.

(E) Gene ontology (GO) enrichment analysis of K504E-white vs K504E-red for BP, CC, and MF categories.

Supplementary Figure S9. Sequence alignment of K. lactis and S. cerevisiae Cdc13.

Amino acid sequences of K. lactis and S. cerevisiae Cdc13 were aligned. Residues that are identical between the two species are highlighted in red, and residues with similar physicochemical properties are highlighted in pink. Alignment was performed using [Clustal Omega].

Supplementary Figure S10. SDS-PAGE analysis of additional proteins used in this study.

Coomassie-stained gels showing the indicated proteins. Molecular weight markers are included.

Supplementary Figure S11. Summary of DNA substrates used in this study.

Diagram summarizing the sequences, lengths, and labeling of DNA substrates employed in the experiments.

Table S1. DNA substrates used in this study.

List of DNA substrates, including sequences, lengths, and labeling information for all oligonucleotides used in experiments.

Table S2. Yeast strains used in this study.

Genotypes of all yeast strains employed in this study, including relevant mutations and background information.

Reference

1 Blackburn, E. H. Structure and function of telomeres. *Nature* **350**, 569-573, doi:10.1038/350569a0 (1991).

2 de Lange, T. Shelterin: the protein complex that shapes and safeguards human telomeres. *Genes Dev* **19**, 2100-2110, doi:10.1101/gad.1346005 (2005).

3 Palm, W. & de Lange, T. How shelterin protects mammalian telomeres. *Annu Rev Genet* **42**, 301-334, doi:10.1146/annurev.genet.41.110306.130350 (2008).

4 Wellinger, R. J. & Zakian, V. A. Everything you ever wanted to know about Saccharomyces cerevisiae telomeres: beginning to end. *Genetics* **191**, 1073-1105, doi:10.1534/genetics.111.137851 (2012).

5 Wu, R. A., Upton, H. E., Vogan, J. M. & Collins, K. Telomerase Mechanism of Telomere Synthesis. *Annu Rev Biochem* **86**, 439-460, doi:10.1146/annurev-biochem-061516-045019 (2017).

6 Gnugge, R. & Symington, L. S. DNA end resection during homologous recombination. *Curr Opin Genet Dev* **71**, 99-105, doi:10.1016/j.gde.2021.07.004 (2021).

7 Symington, L. S. Mechanism and regulation of DNA end resection in eukaryotes. *Crit Rev Biochem Mol Biol* **51**, 195-212, doi:10.3109/10409238.2016.1172552 (2016).
8 Wu, P., Takai, H. & de Lange, T. Telomeric 3' overhangs derive from resection by Exo1 and Apollo and fill-in by POT1b-associated CST. *Cell* **150**, 39-52, doi:10.1016/j.cell.2012.05.026 (2012).
9 Claussin, C. & Chang, M. The many facets of homologous recombination at telomeres. *Microb Cell* **2**, 308-321, doi:10.15698/mic2015.09.224 (2015).
10 Bonetti, D., Martina, M., Clerici, M., Lucchini, G. & Longhese, M. P. Multiple pathways regulate 3' overhang generation at S. cerevisiae telomeres. *Mol Cell* **35**, 70-81, doi:10.1016/j.molcel.2009.05.015 (2009).
11 Symington, L. S. & Gautier, J. Double-strand break end resection and repair pathway choice. *Annu Rev Genet* **45**, 247-271, doi:10.1146/annurev-genet-110410-132435 (2011).
12 Mimitou, E. P. & Symington, L. S. DNA end resection: many nucleases make light work. *DNA Repair (Amst)* **8**, 983-995, doi:10.1016/j.dnarep.2009.04.017 (2009).
13 Ngo, H. P. & Lydall, D. Survival and growth of yeast without telomere capping by Cdc13 in the absence of Sgs1, Exo1, and Rad9. *PLoS Genet* **6**, e1001072, doi:10.1371/journal.pgen.1001072 (2010).
14 Linger, B. R. & Price, C. M. Conservation of telomere protein complexes: shuffling through evolution. *Crit Rev Biochem Mol Biol* **44**, 434-446, doi:10.3109/10409230903307329 (2009).
15 Wotton, D. & Shore, D. A novel Rap1p-interacting factor, Rif2p, cooperates with Rif1p to regulate telomere length in Saccharomyces cerevisiae. *Genes Dev* **11**, 748-760, doi:10.1101/gad.11.6.748 (1997).
16 Li, B. & de Lange, T. Rap1 affects the length and heterogeneity of human telomeres. *Mol Biol Cell* **14**, 5060-5068, doi:10.1091/mbc.e03-06-0403 (2003).
17 Boulton, S. J. & Jackson, S. P. Components of the Ku-dependent non-homologous end-joining pathway are involved in telomeric length maintenance and telomeric silencing. *EMBO J* **17**, 1819-1828, doi:10.1093/emboj/17.6.1819 (1998).
18 Fouquerel, E., Parikh, D. & Opresko, P. DNA damage processing at telomeres: The ends justify the means. *DNA Repair (Amst)* **44**, 159-168, doi:10.1016/j.dnarep.2016.05.022 (2016).
19 Polotnianka, R. M., Li, J. & Lustig, A. J. The yeast Ku heterodimer is essential for protection of the telomere against nucleolytic and recombinational activities. *Curr Biol* **8**, 831-834, doi:10.1016/s0960-9822(98)70325-2 (1998).
20 Larcher, M. V., Pasquier, E., MacDonald, R. S. & Wellinger, R. J. Ku Binding on Telomeres Occurs at Sites Distal from the Physical Chromosome Ends. *PLoS Genet* **12**, e1006479, doi:10.1371/journal.pgen.1006479 (2016).
21 Williams, J. M., Ouenzar, F., Lemon, L. D., Chartrand, P. & Bertuch, A. A. The principal role of Ku in telomere length maintenance is promotion of Est1 association with telomeres. *Genetics* **197**, 1123-1136, doi:10.1534/genetics.114.164707 (2014).

22 Boulton, S. J. & Jackson, S. P. Saccharomyces cerevisiae Ku70 potentiates illegitimate DNA double-strand break repair and serves as a barrier to error-prone DNA repair pathways. *EMBO J* **15**, 5093-5103 (1996).
23 Abbasi, S., Parmar, G., Kelly, R. D., Balasuriya, N. & Schild-Poulter, C. The Ku complex: recent advances and emerging roles outside of non-homologous end-joining. *Cell Mol Life Sci* **78**, 4589-4613, doi:10.1007/s00018-021-03801-1 (2021).
24 Chandra, A., Hughes, T. R., Nugent, C. I. & Lundblad, V. Cdc13 both positively and negatively regulates telomere replication. *Genes Dev* **15**, 404-414, doi:10.1101/gad.861001 (2001).
25 Hughes, T. R., Weilbaecher, R. G., Walterscheid, M. & Lundblad, V. Identification of the single-strand telomeric DNA binding domain of the Saccharomyces cerevisiae Cdc13 protein. *Proc Natl Acad Sci U S A* **97**, 6457-6462, doi:10.1073/pnas.97.12.6457 (2000).
26 Sun, J. *et al.* Structural bases of dimerization of yeast telomere protein Cdc13 and its interaction with the catalytic subunit of DNA polymerase alpha. *Cell Res* **21**, 258-274, doi:10.1038/cr.2010.138 (2011).
27 Mitchell, M. T. *et al.* Cdc13 N-terminal dimerization, DNA binding, and telomere length regulation. *Mol Cell Biol* **30**, 5325-5334, doi:10.1128/MCB.00515-10 (2010).
28 Nugent, C. I., Hughes, T. R., Lue, N. F. & Lundblad, V. Cdc13p: a single-strand telomeric DNA-binding protein with a dual role in yeast telomere maintenance. *Science* **274**, 249-252, doi:10.1126/science.274.5285.249 (1996).
29 Lin, J. J. & Zakian, V. A. The Saccharomyces CDC13 protein is a single-strand TG1-3 telomeric DNA-binding protein in vitro that affects telomere behavior in vivo. *Proc Natl Acad Sci U S A* **93**, 13760-13765, doi:10.1073/pnas.93.24.13760 (1996).
30 Miyake, Y. *et al.* RPA-like mammalian Ctc1-Stn1-Ten1 complex binds to single-stranded DNA and protects telomeres independently of the Pot1 pathway. *Mol Cell* **36**, 193-206, doi:10.1016/j.molcel.2009.08.009 (2009).
31 Chen, L. Y., Redon, S. & Lingner, J. The human CST complex is a terminator of telomerase activity. *Nature* **488**, 540-544, doi:10.1038/nature11269 (2012).
32 Stewart, J. A. *et al.* Human CST promotes telomere duplex replication and general replication restart after fork stalling. *EMBO J* **31**, 3537-3549, doi:10.1038/emboj.2012.215 (2012).
33 Wang, L. *et al.* Pan-Cancer Analyses Identify the CTC1-STN1-TEN1 Complex as a Protective Factor and Predictive Biomarker for Immune Checkpoint Blockade in Cancer. *Front Genet* **13**, 859617, doi:10.3389/fgene.2022.859617 (2022).
34 Lyu, X., Sang, P. B. & Chai, W. CST in maintaining genome stability: Beyond telomeres. *DNA Repair (Amst)* **102**, 103104, doi:10.1016/j.dnarep.2021.103104 (2021).
35 Cai, S. W. & de Lange, T. CST-Polalpha/Primase: the second telomere maintenance machine. *Genes Dev* **37**, 555-569, doi:10.1101/gad.350479.123 (2023).
36 Rice, C. & Skordalakes, E. Structure and function of the telomeric CST complex. *Comput Struct Biotechnol J* **14**, 161-167, doi:10.1016/j.csbj.2016.04.002 (2016).

37 Greider, C. W. Telomerase activity, cell proliferation, and cancer. *Proc Natl Acad Sci U S A* **95**, 90-92, doi:10.1073/pnas.95.1.90 (1998).
38 Bhattacharjee, A., Wang, Y., Diao, J. & Price, C. M. Dynamic DNA binding, junction recognition and G4 melting activity underlie the telomeric and genome-wide roles of human CST. *Nucleic Acids Res* **45**, 12311-12324, doi:10.1093/nar/gkx878 (2017).
39 Lewis, K. A., Pfaff, D. A., Earley, J. N., Altschuler, S. E. & Wuttke, D. S. The tenacious recognition of yeast telomere sequence by Cdc13 is fully exerted by a single OB-fold domain. *Nucleic Acids Res* **42**, 475-484, doi:10.1093/nar/gkt843 (2014).
40 Anderson, E. M., Halsey, W. A. & Wuttke, D. S. Delineation of the high-affinity single-stranded telomeric DNA-binding domain of Saccharomyces cerevisiae Cdc13. *Nucleic Acids Res* **30**, 4305-4313, doi:10.1093/nar/gkf554 (2002).
41 Alani, E., Thresher, R., Griffith, J. D. & Kolodner, R. D. Characterization of DNA-binding and strand-exchange stimulation properties of y-RPA, a yeast single-strand-DNA-binding protein. *J Mol Biol* **227**, 54-71, doi:10.1016/0022-2836(92)90681-9 (1992).
42 Ge, Y. *et al.* Structural insights into telomere protection and homeostasis regulation by yeast CST complex. *Nat Struct Mol Biol* **27**, 752-762, doi:10.1038/s41594-020-0459-8 (2020).
43 Mitton-Fry, R. M., Anderson, E. M., Theobald, D. L., Glustrom, L. W. & Wuttke, D. S. Structural basis for telomeric single-stranded DNA recognition by yeast Cdc13. *J Mol Biol* **338**, 241-255, doi:10.1016/j.jmb.2004.01.063 (2004).
44 Chen, Y. F. *et al.* Modulation of yeast telomerase activity by Cdc13 and Est1 in vitro. *Sci Rep* **6**, 34104, doi:10.1038/srep34104 (2016).
45 Cejka, P. *et al.* DNA end resection by Dna2-Sgs1-RPA and its stimulation by Top3-Rmi1 and Mre11-Rad50-Xrs2. *Nature* **467**, 112-116, doi:10.1038/nature09355 (2010).
46 Kasaciunaite, K. *et al.* Competing interaction partners modulate the activity of Sgs1 helicase during DNA end resection. *EMBO J* **38**, e101516, doi:10.15252/embj.2019101516 (2019).
47 Shen, J. *et al.* Deciphering the mechanism of processive ssDNA digestion by the Dna2-RPA ensemble. *Nat Commun* **13**, 359, doi:10.1038/s41467-021-27940-y (2022).
48 Krasner, D. S., Daley, J. M., Sung, P. & Niu, H. Interplay between Ku and Replication Protein A in the Restriction of Exo1-mediated DNA Break End Resection. *J Biol Chem* **290**, 18806-18816, doi:10.1074/jbc.M115.660191 (2015).
49 Lopez, C. R. *et al.* Ku must load directly onto the chromosome end in order to mediate its telomeric functions. *PLoS Genet* **7**, e1002233, doi:10.1371/journal.pgen.1002233 (2011).
50 Maringele, L. & Lydall, D. EXO1-dependent single-stranded DNA at telomeres activates subsets of DNA damage and spindle checkpoint pathways in budding yeast yku70Delta mutants. *Genes Dev* **16**, 1919-1933, doi:10.1101/gad.225102 (2002).
51 Frey, M. W., Sowers, L. C., Millar, D. P. & Benkovic, S. J. The nucleotide analog 2-aminopurine as a spectroscopic probe of nucleotide incorporation by the

Klenow fragment of Escherichia coli polymerase I and bacteriophage T4 DNA polymerase. *Biochemistry* **34**, 9185-9192, doi:10.1021/bi00028a031 (1995).
52 Jean, J. M. & Hall, K. B. 2-Aminopurine fluorescence quenching and lifetimes: role of base stacking. *Proc Natl Acad Sci U S A* **98**, 37-41, doi:10.1073/pnas.98.1.37 (2001).
53 Wu, T. J. *et al.* Sequential loading of Saccharomyces cerevisiae Ku and Cdc13p to telomeres. *J Biol Chem* **284**, 12801-12808, doi:10.1074/jbc.M809131200 (2009).
54 Tong, X. J. *et al.* Est1 protects telomeres and inhibits subtelomeric y'-element recombination. *Mol Cell Biol* **31**, 1263-1274, doi:10.1128/MCB.00831-10 (2011).
55 Hardy, J., Churikov, D., Geli, V. & Simon, M. N. Sgs1 and Sae2 promote telomere replication by limiting accumulation of ssDNA. *Nat Commun* **5**, 5004, doi:10.1038/ncomms6004 (2014).
56 Boulton, S. J. & Jackson, S. P. Identification of a Saccharomyces cerevisiae Ku80 homologue: roles in DNA double strand break rejoining and in telomeric maintenance. *Nucleic Acids Res* **24**, 4639-4648, doi:10.1093/nar/24.23.4639 (1996).
57 Bertuch, A. A. & Lundblad, V. The Ku heterodimer performs separable activities at double-strand breaks and chromosome termini. *Mol Cell Biol* **23**, 8202-8215, doi:10.1128/MCB.23.22.8202-8215.2003 (2003).
58 Ljungdahl, P. O. & Daignan-Fornier, B. Regulation of amino acid, nucleotide, and phosphate metabolism in Saccharomyces cerevisiae. *Genetics* **190**, 885-929, doi:10.1534/genetics.111.133306 (2012).
59 Dorfman, B. Z. The isolation of adenylosuccinate synthetase mutants in yeast by selection for constitutive behavior in pigmented strains. *Genetics* **61**, 377-389, doi:10.1093/genetics/61.2.377 (1969).
60 Tesmer, V. M., Brenner, K. A. & Nandakumar, J. Human POT1 protects the telomeric ds-ss DNA junction by capping the 5' end of the chromosome. *Science* **381**, 771-778, doi:10.1126/science.adi2436 (2023).
61 Lei, M., Podell, E. R. & Cech, T. R. Structure of human POT1 bound to telomeric single-stranded DNA provides a model for chromosome end-protection. *Nat Struct Mol Biol* **11**, 1223-1229, doi:10.1038/nsmb867 (2004).

Figure 1

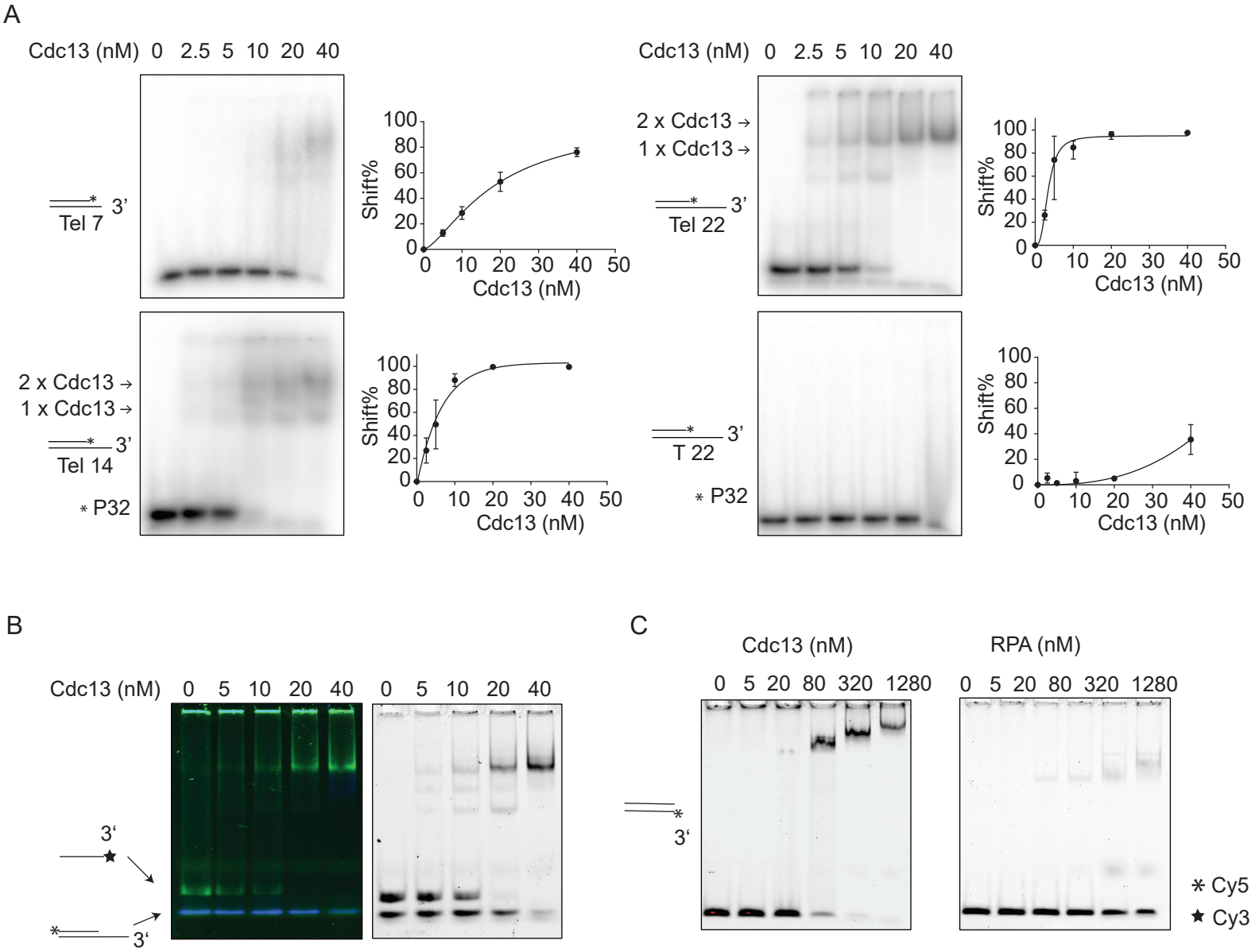
A
Cdc13 (nM) 0 2.5 5 10 20 40
Tel 7
3'
Shift%
Cdc13 (nM)
2 x Cdc13
1 x Cdc13
Tel 14
P32
Tel 22
T 22
B
Cdc13 (nM) 0 5 10 20 40 0 5 10 20 40
3'
C
Cdc13 (nM)
RPA (nM)
0 5 20 80 320 1280
Cy5
Cy3

Figure 2

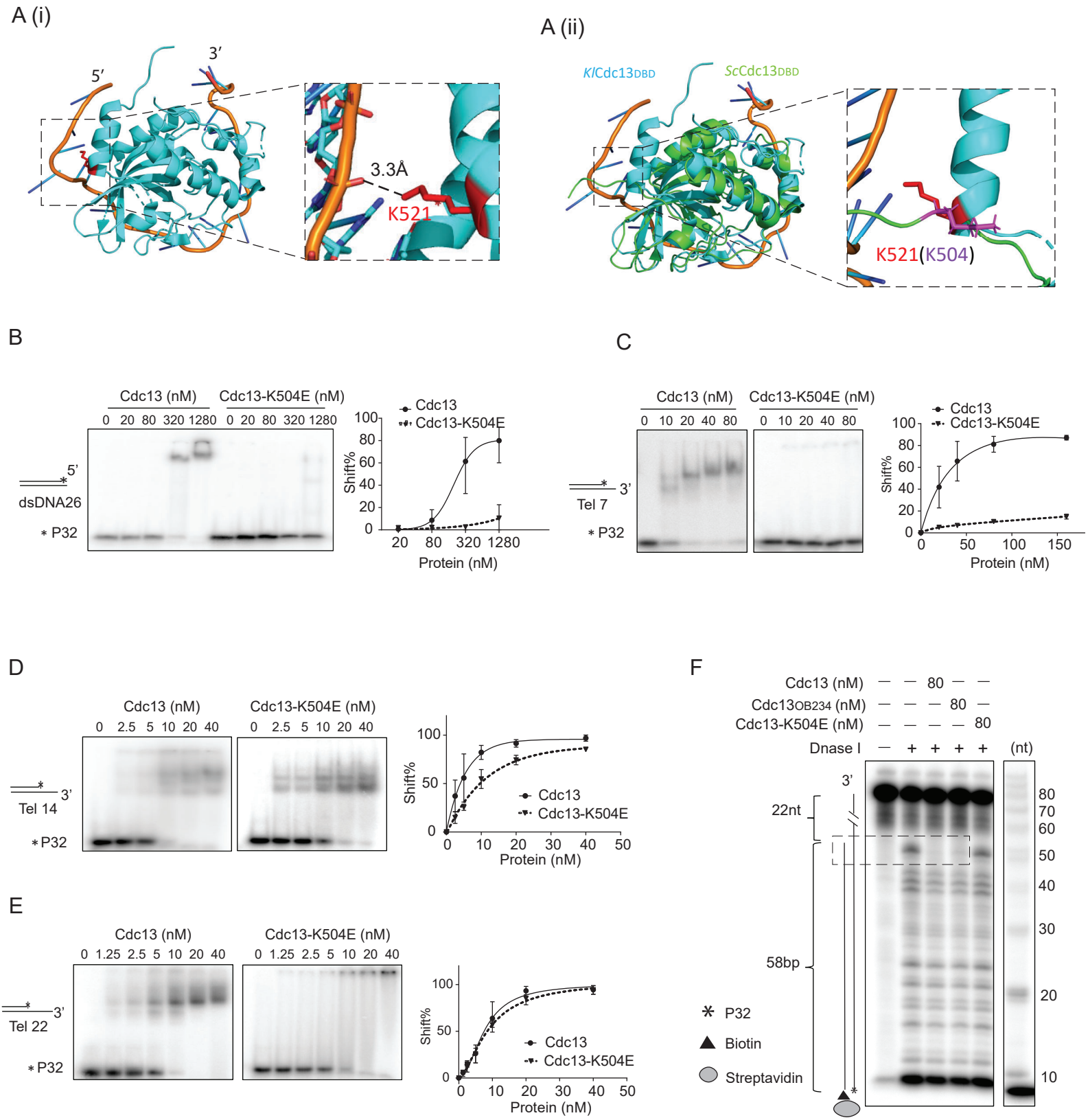
A (i)
5′
3′
3.3Å
K521
A (ii)
KlCdc13DBD
ScCdc13DBD
K521(K504)
B
Cdc13 (nM)
Cdc13-K504E (nM)
0 20 80 320 1280 0 20 80 320 1280
5′
dsDNA26
* P32
Cdc13
Cdc13-K504E
Shift%
Protein (nM)
C
Cdc13 (nM)
Cdc13-K504E (nM)
0 10 20 40 80 0 10 20 40 80
3′
Tel 7
* P32
Cdc13
Cdc13-K504E
Shift%
Protein (nM)
D
Cdc13 (nM)
Cdc13-K504E (nM)
0 2.5 5 10 20 40 0 2.5 5 10 20 40
3′
Tel 14
* P32
Cdc13
Cdc13-K504E
Shift%
Protein (nM)
E
Cdc13 (nM)
Cdc13-K504E (nM)
0 1.25 2.5 5 10 20 40 0 1.25 2.5 5 10 20 40
3′
Tel 22
* P32
Cdc13
Cdc13-K504E
Shift%
Protein (nM)
F
Cdc13 (nM) — — 80 — —
Cdc13OB234 (nM) — — — 80 —
Cdc13-K504E (nM) — — — — 80
Dnase I — + + + +
(nt)
3′
22nt
58bp
* P32
Biotin
Streptavidin
80
70
60
50
40
30
20
10

Figure 3

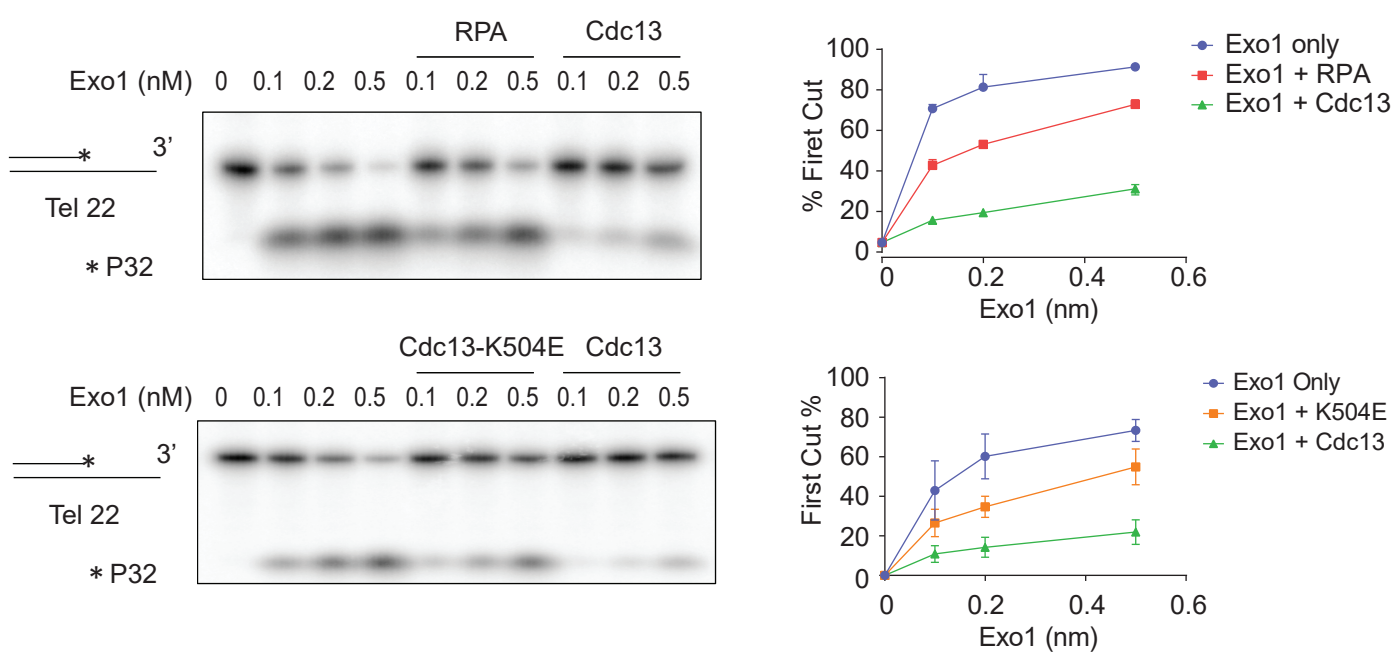

Figure 4

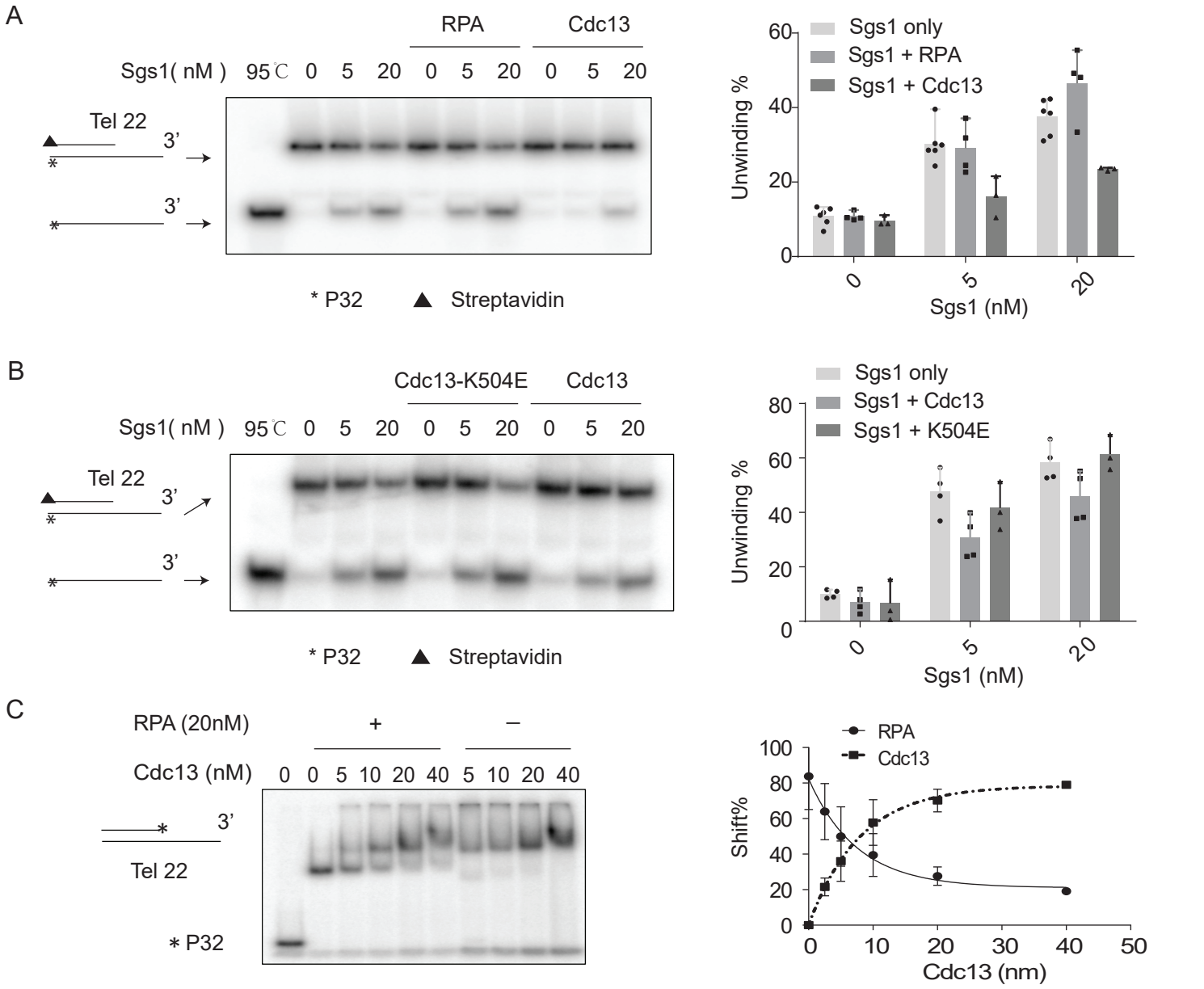

Figure 5

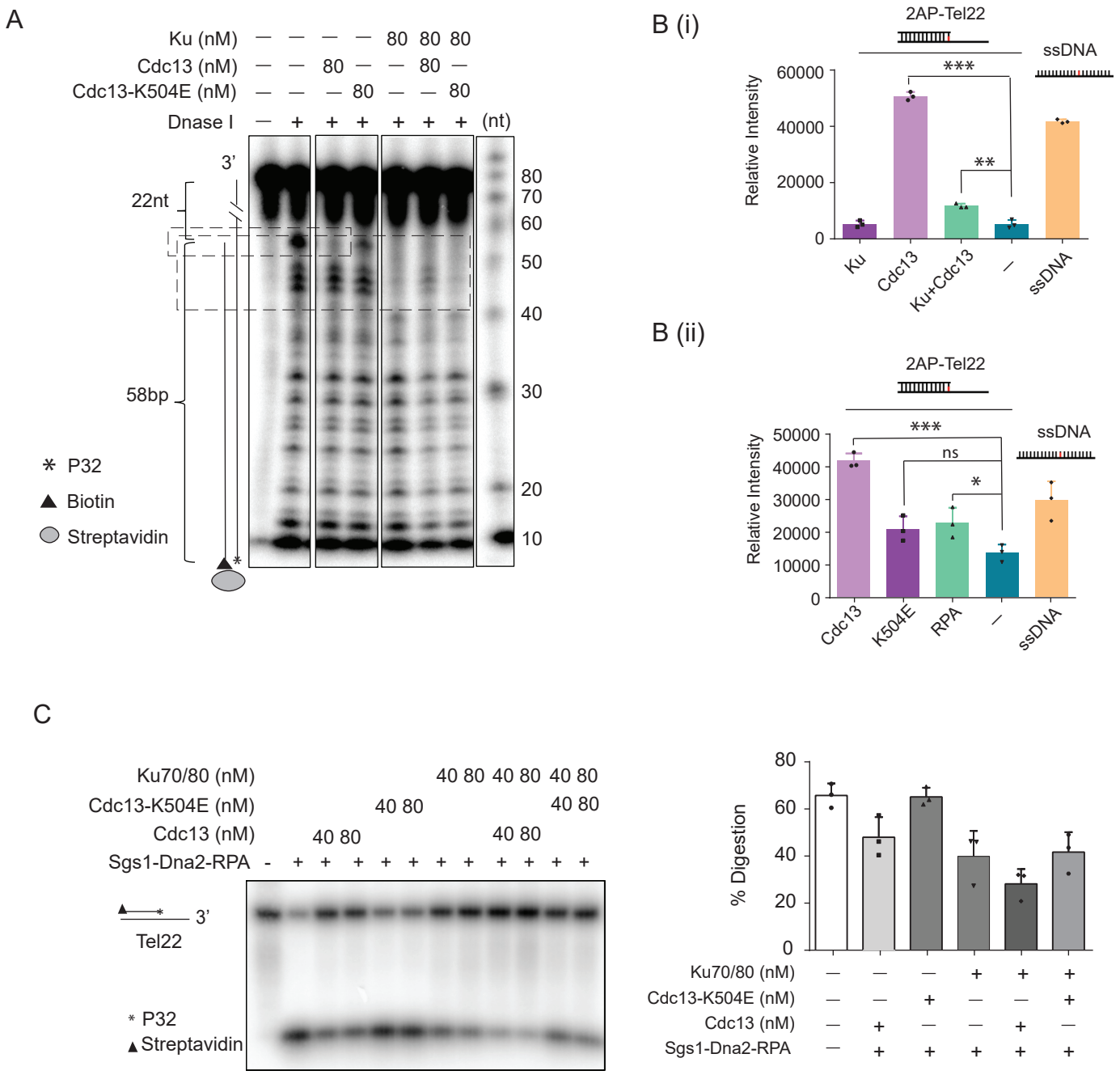
A
Ku (nM)
Cdc13 (nM)
Cdc13-K504E (nM)
Dnase I
(nt)
3'
22nt
58bp
80
70
60
50
40
30
20
10
P32
Biotin
Streptavidin
B (i)
2AP-Tel22
ssDNA
Relative Intensity
60000
40000
20000
0
***
**
Ku
Cdc13
Ku+Cdc13
–
ssDNA
B (ii)
2AP-Tel22
ssDNA
Relative Intensity
50000
40000
30000
20000
10000
0
***
ns
*
Cdc13
K504E
RPA
–
ssDNA
C
Ku70/80 (nM)
Cdc13-K504E (nM)
Cdc13 (nM)
Sgs1-Dna2-RPA
3'
Tel22
P32
Streptavidin
% Digestion
80
60
40
20
0
Ku70/80 (nM)
Cdc13-K504E (nM)
Cdc13 (nM)
Sgs1-Dna2-RPA

Figure 6

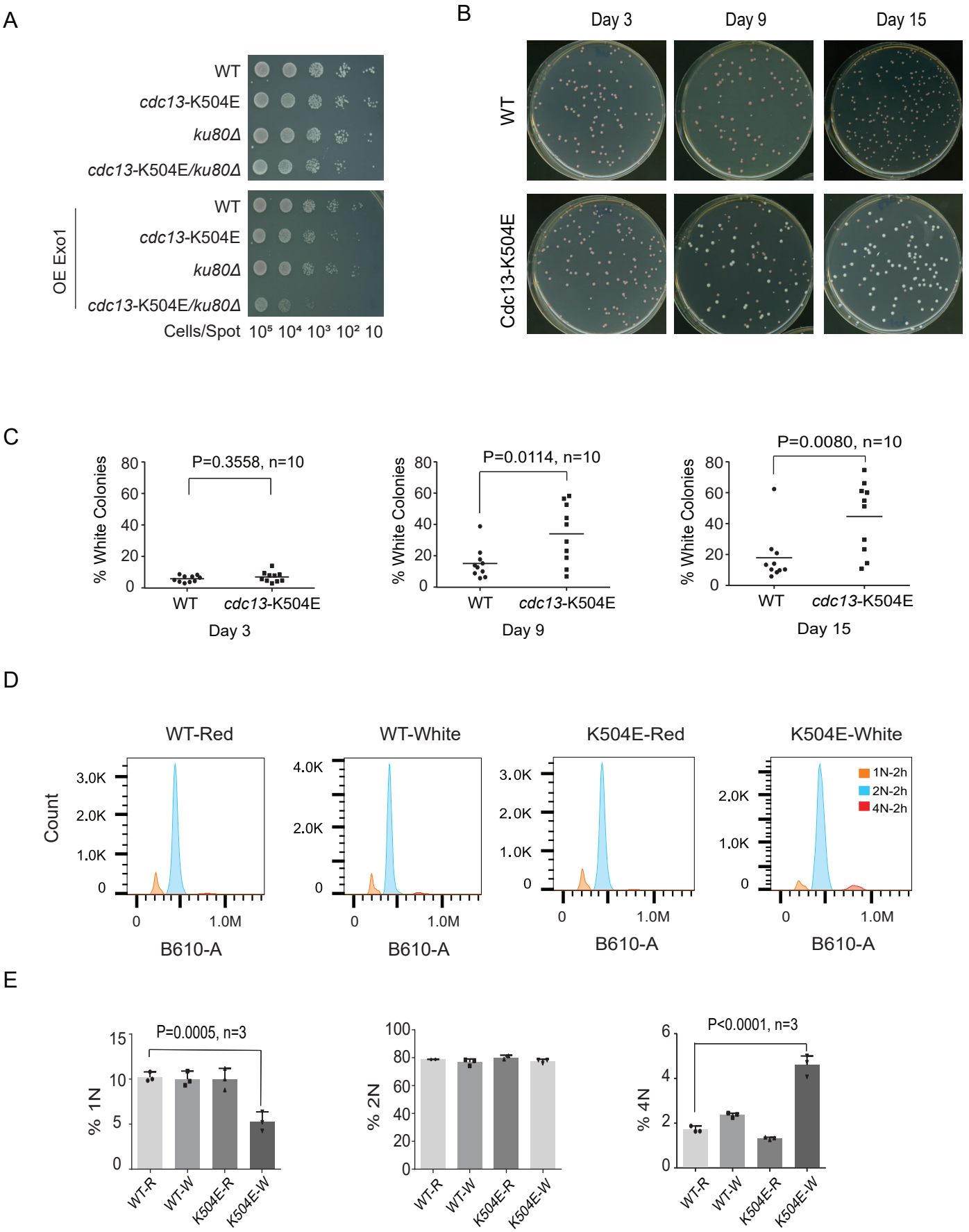
A
WT
cdc13-K504E
ku80Δ
cdc13-K504E/ku80Δ
OE Exo1
WT
cdc13-K504E
ku80Δ
cdc13-K504E/ku80Δ
Cells/Spot 10⁵ 10⁴ 10³ 10² 10
B
Day 3
Day 9
Day 15
WT
Cdc13-K504E
C
% White Colonies
P=0.3558, n=10
WT
cdc13-K504E
Day 3
P=0.0114, n=10
Day 9
P=0.0080, n=10
Day 15
D
WT-Red
WT-White
K504E-Red
K504E-White
Count
B610-A
1N-2h
2N-2h
4N-2h
E
% 1N
P=0.0005, n=3
% 2N
% 4N
P<0.0001, n=3
WT-R
WT-W
K504E-R
K504E-W

Figure 7

A

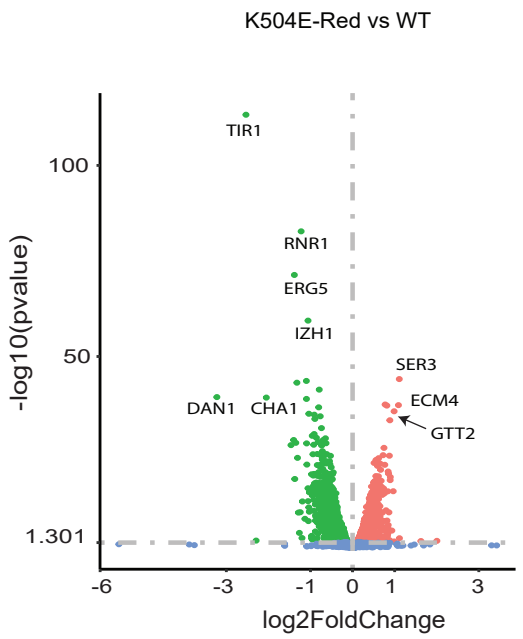
K504E-Red vs WT
-log10(pvalue)
log2FoldChange
100
50
1.301
-6
-3
-1
0
1
3
TIR1
RNR1
ERG5
IZH1
SER3
ECM4
GTT2
DAN1
CHA1

B

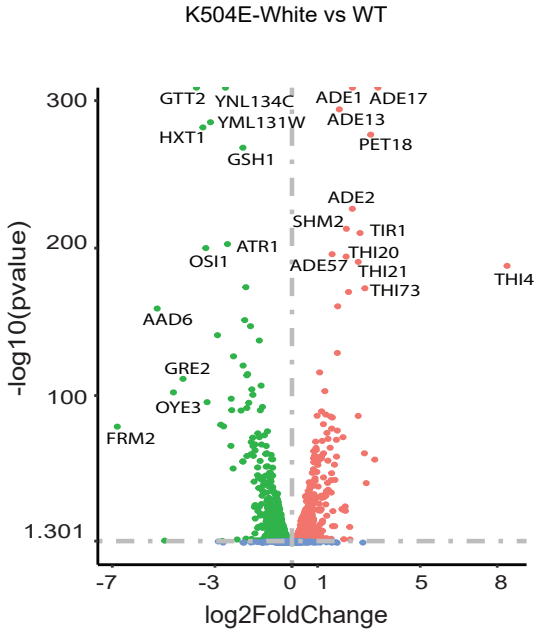
K504E-White vs WT
-log10(pvalue)
log2FoldChange
300
200
100
1.301
-7
-3
0
1
5
8
GTT2
YNL134C
YML131W
HXT1
GSH1
ADE1
ADE17
ADE13
PET18
ADE2
SHM2
TIR1
ATR1
OSI1
THI20
ADE57
THI21
THI73
THI4
AAD6
GRE2
OYE3
FRM2

C

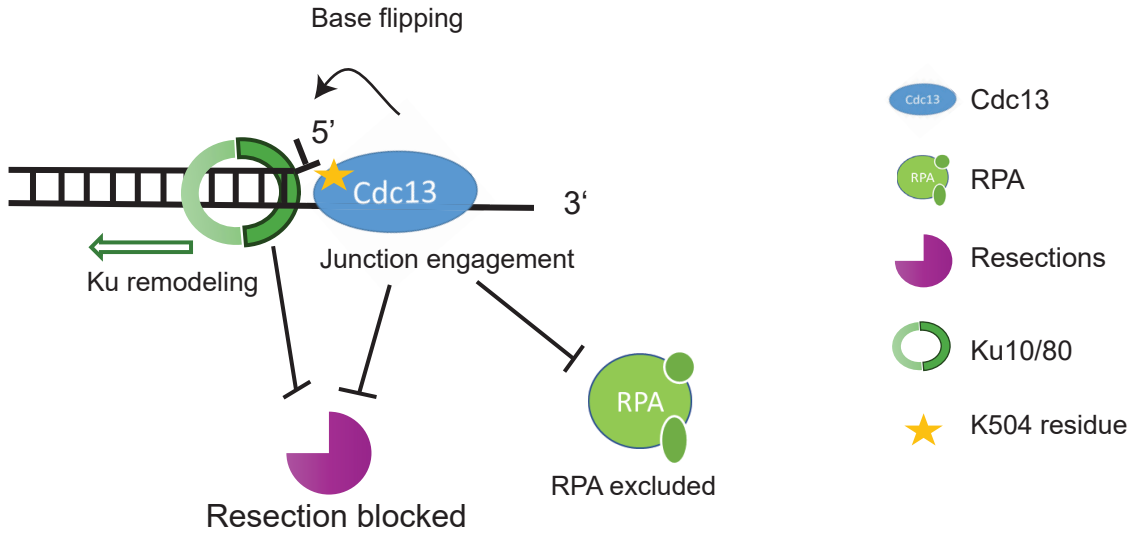
Base flipping
5'
3'
Cdc13
Ku remodeling
Junction engagement
Resection blocked
RPA
RPA excluded
Cdc13
RPA
Resections
Ku10/80
K504 residue

Figure S1

A

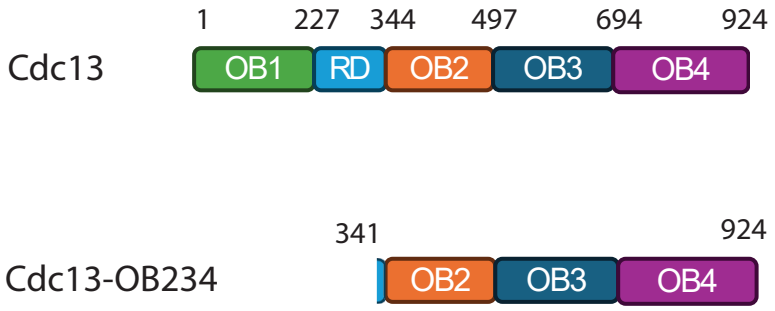

B

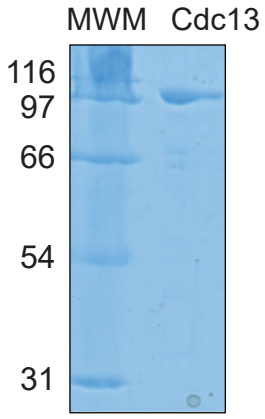

C

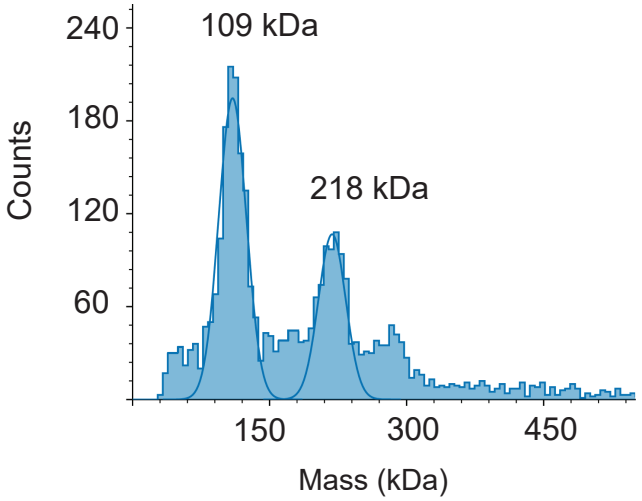

D

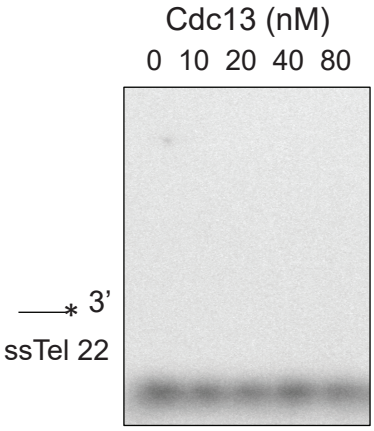

Figure S2

A

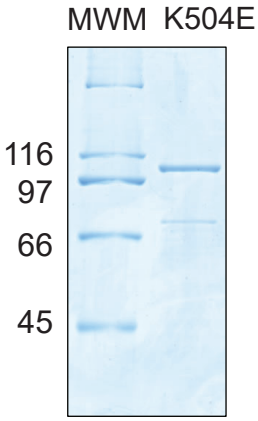

B

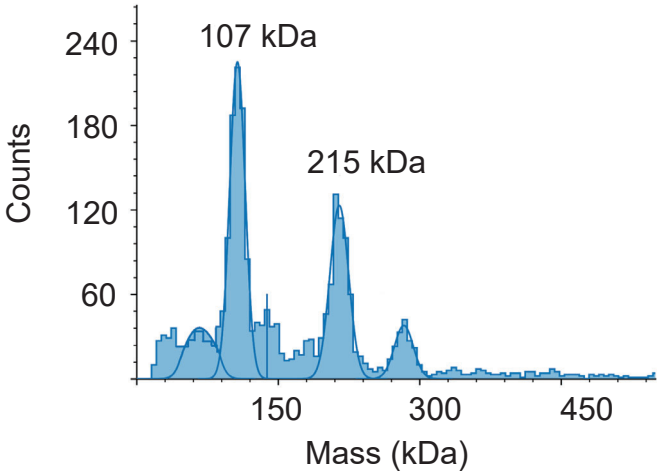

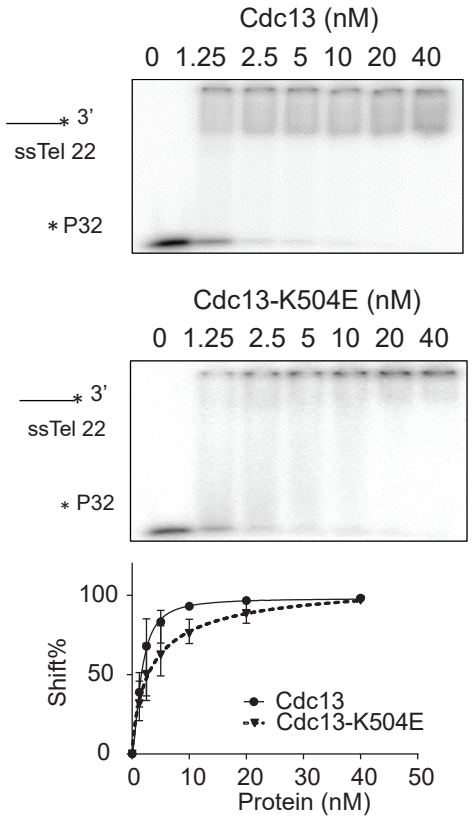
C
Cdc13 (nM)
0 1.25 2.5 5 10 20 40
3'
ssTel 22
P32
Cdc13-K504E (nM)
0 1.25 2.5 5 10 20 40
3'
ssTel 22
P32
Shift%
100
50
0
0 10 20 30 40 50
Protein (nM)
Cdc13
Cdc13-K504E

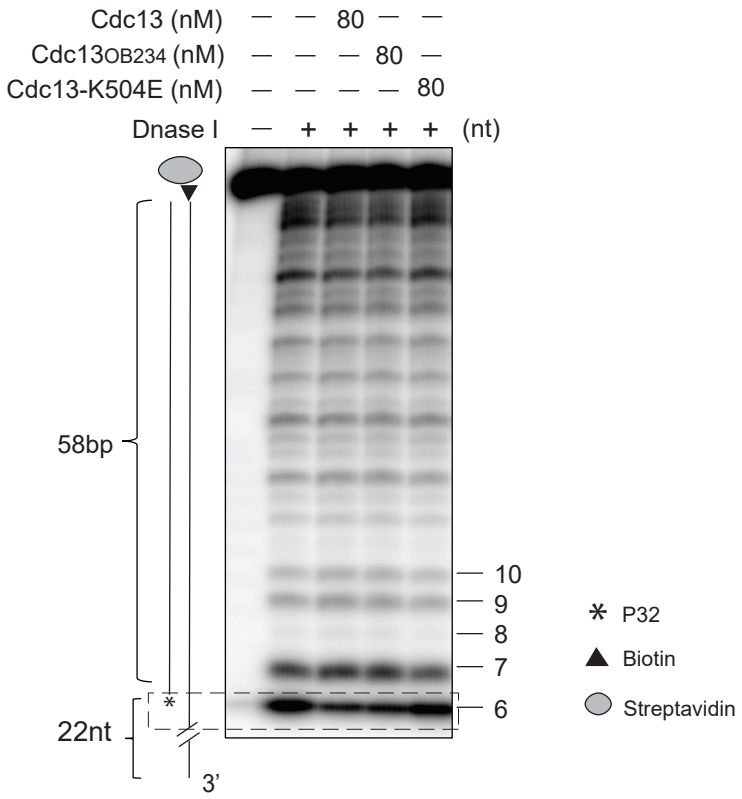
D
Cdc13 (nM) — — 80 — —
Cdc13OB234 (nM) — — — 80 —
Cdc13-K504E (nM) — — — — 80
Dnase I — + + + + (nt)
58bp
22nt
3'
10
9
8
7
6
P32
Biotin
Streptavidin

Figure S3

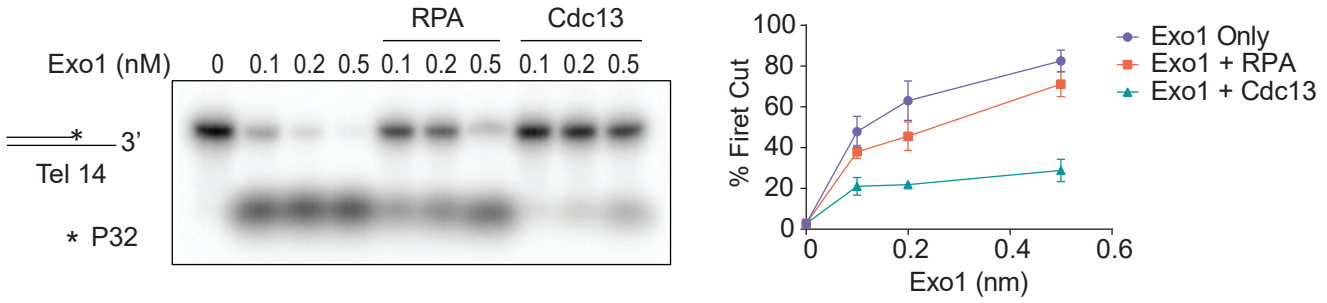
A (i)
RPA
Cdc13
Exo1 (nM) 0 0.1 0.2 0.5 0.1 0.2 0.5 0.1 0.2 0.5
3'
Tel 14
P32
% Firet Cut
100
80
60
40
20
0
0 0.2 0.4 0.6
Exo1 (nm)
Exo1 Only
Exo1 + RPA
Exo1 + Cdc13

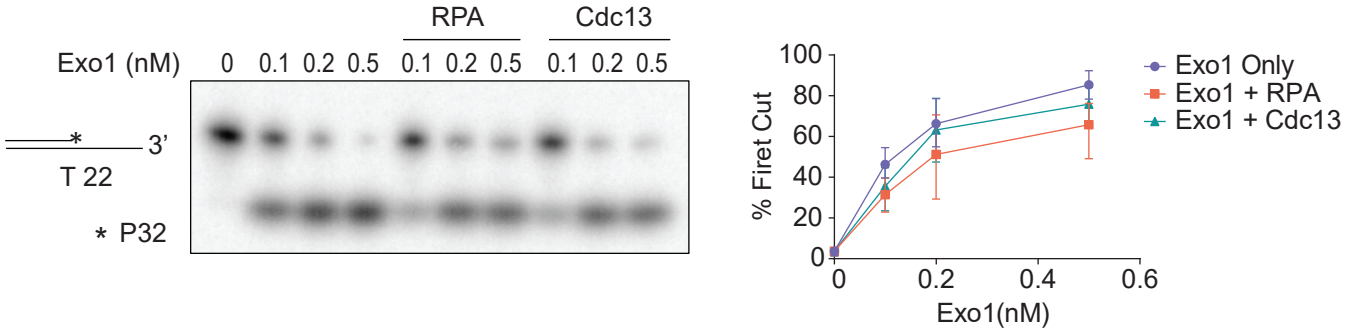
A (ii)
RPA
Cdc13
Exo1 (nM) 0 0.1 0.2 0.5 0.1 0.2 0.5 0.1 0.2 0.5
3'
T 22
P32
% Firet Cut
100
80
60
40
20
0
0 0.2 0.4 0.6
Exo1(nM)
Exo1 Only
Exo1 + RPA
Exo1 + Cdc13

B

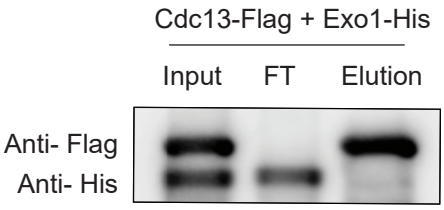

C

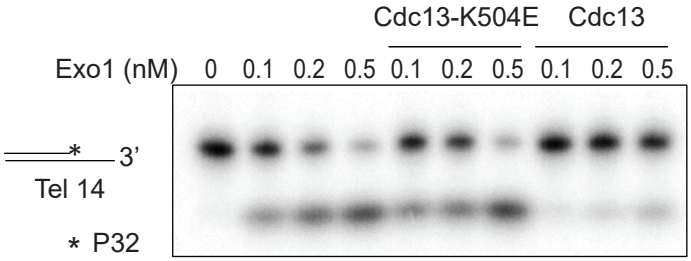

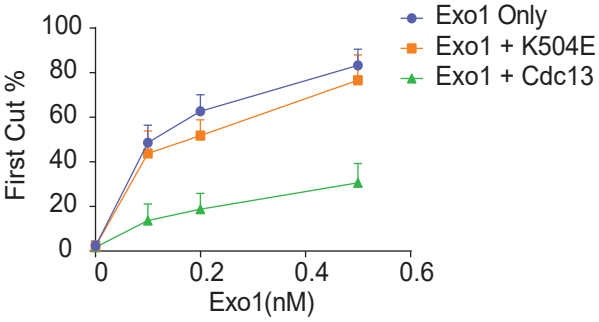

Figure S4

A (i)

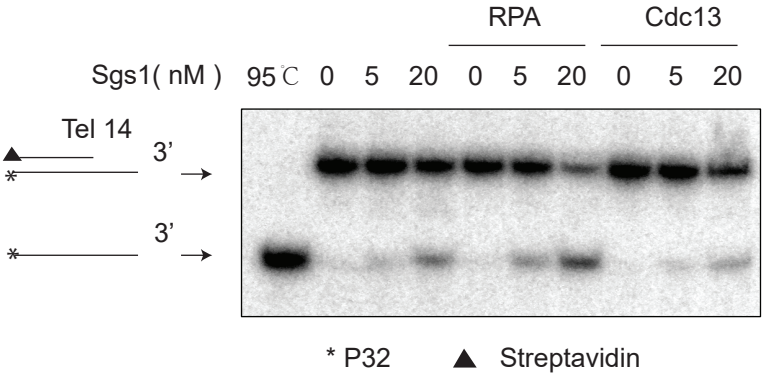

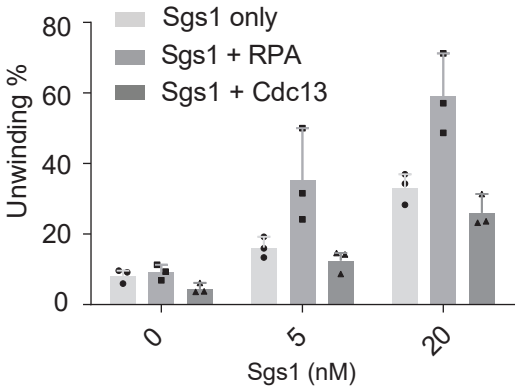

A (ii)

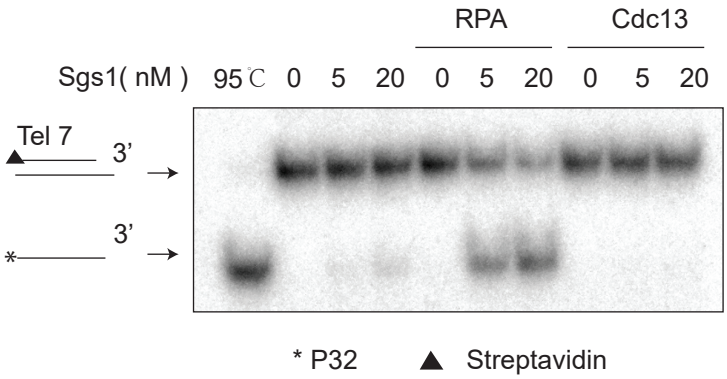

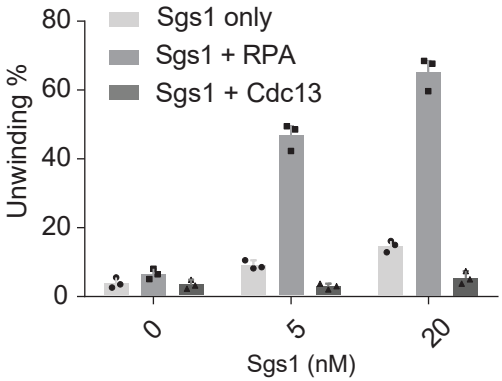

B

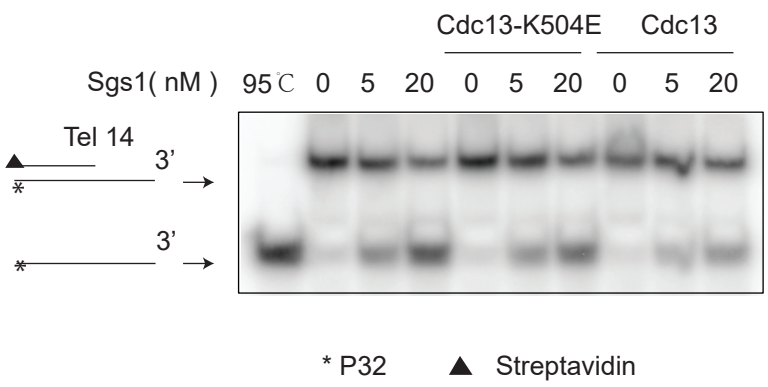

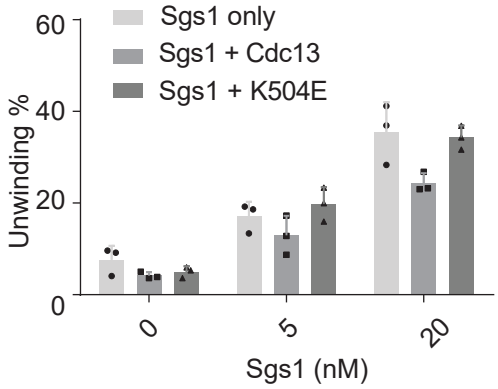

C (i)

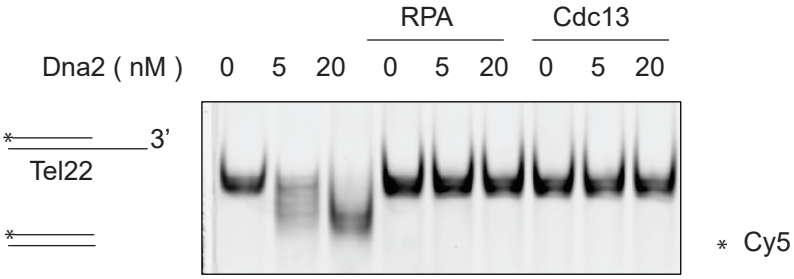

C (ii)

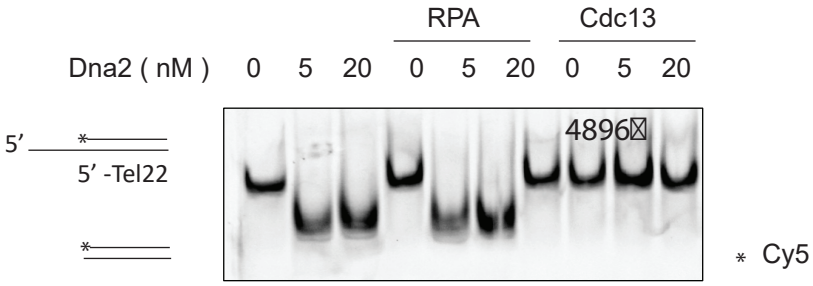

C (iii)

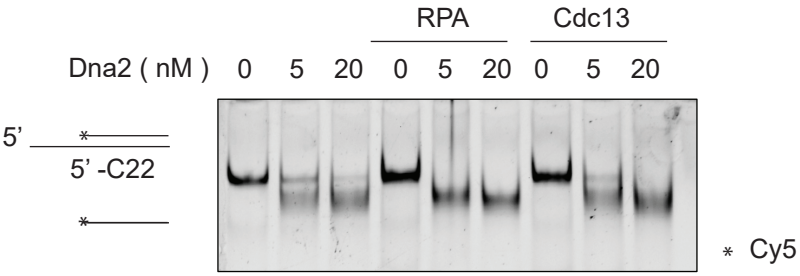

D

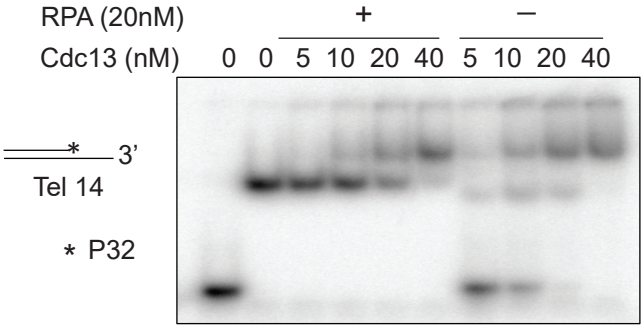

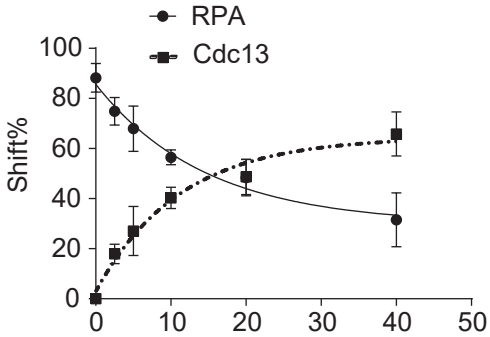

Figure S5

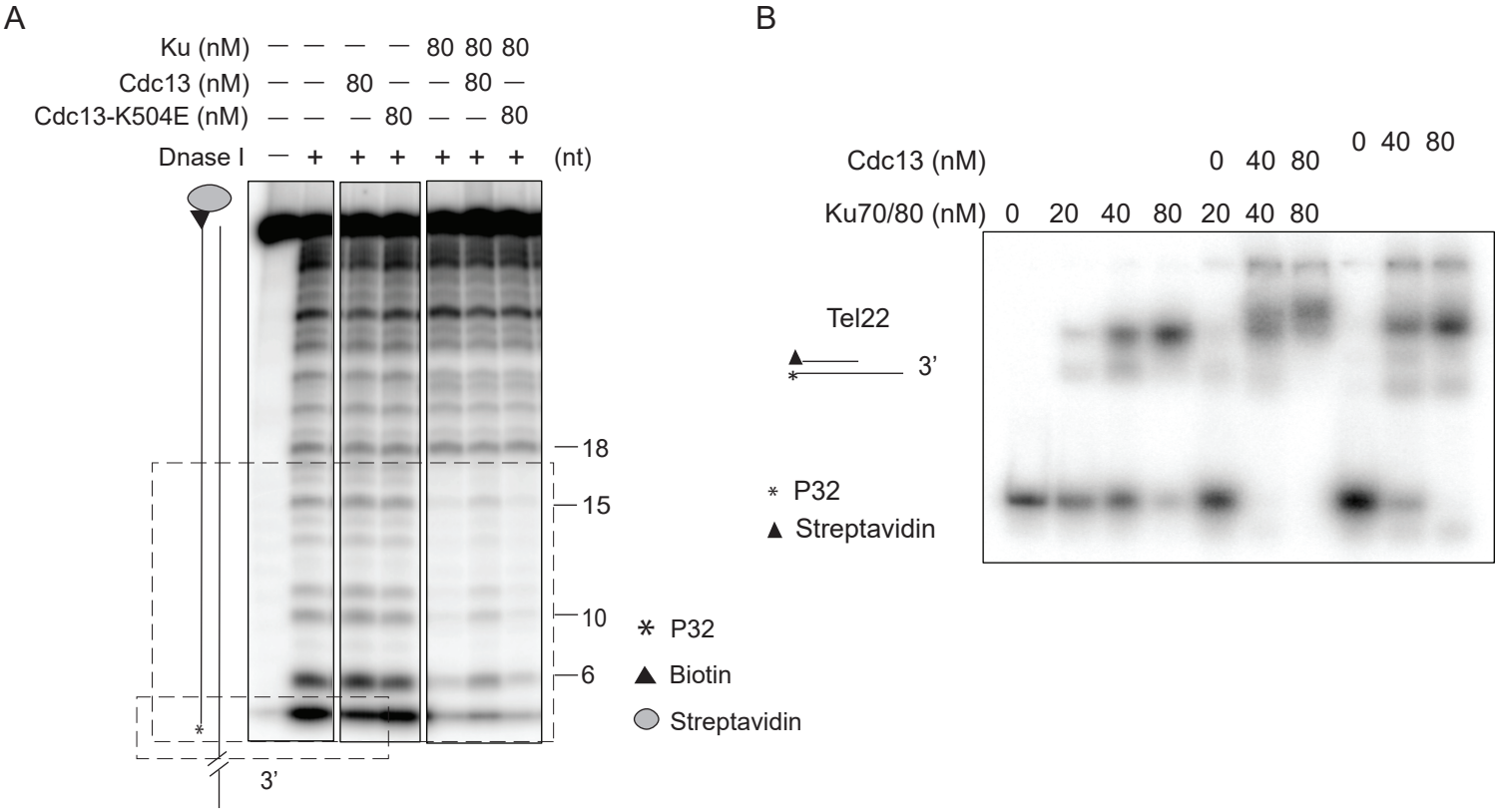

Figure S6

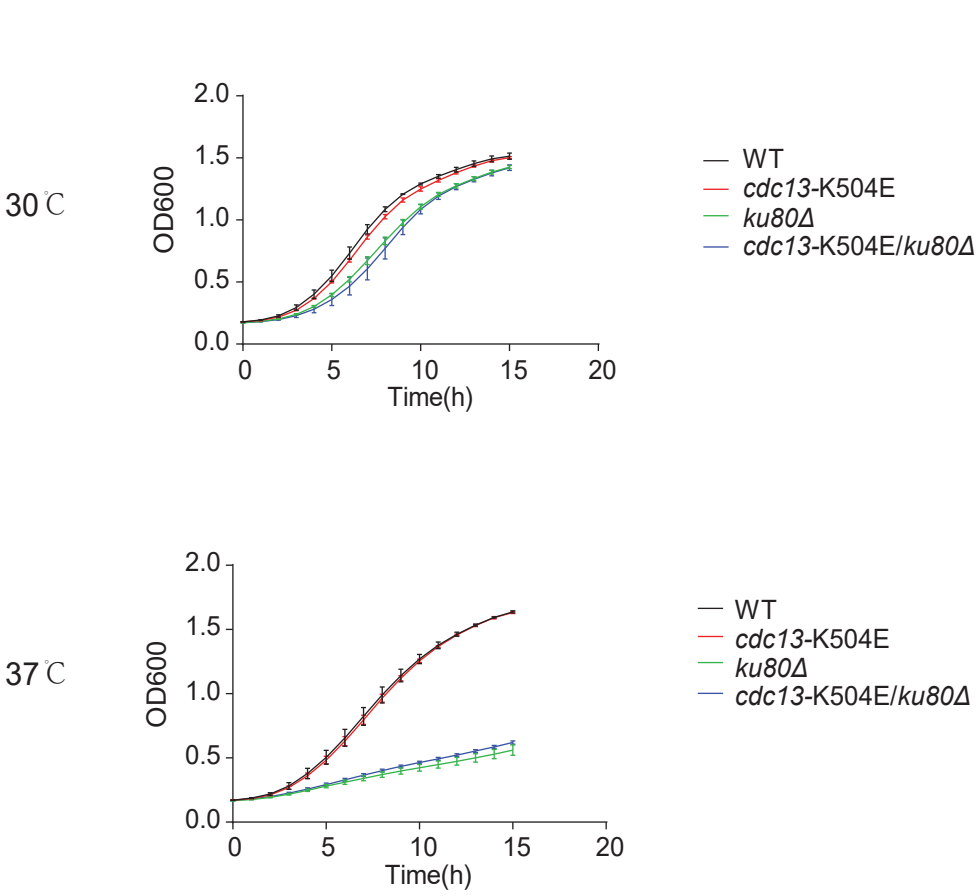

B

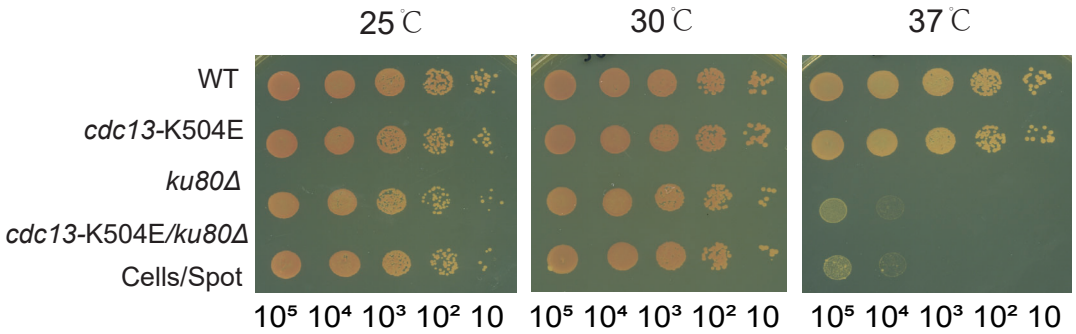
25℃
30℃
37℃
WT
cdc13-K504E
ku80Δ
cdc13-K504E/ku80Δ
Cells/Spot
10⁵ 10⁴ 10³ 10² 10
10⁵ 10⁴ 10³ 10² 10
10⁵ 10⁴ 10³ 10² 10

C

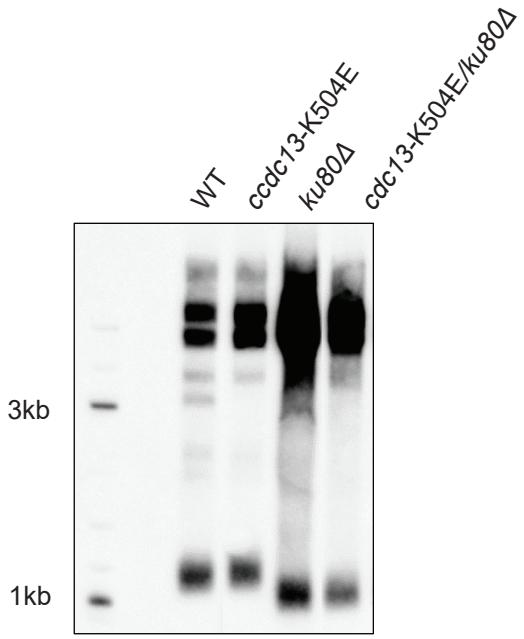
WT
ccdc13-K504E
ku80Δ
cdc13-K504E/ku80Δ
3kb
1kb

D

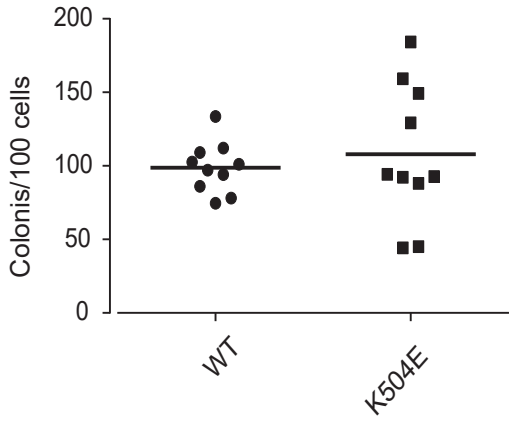
Colonis/100 cells
200
150
100
50
0
WT
K504E

E

Codon 64
WT-Ade2 AAAAACTAGCTGAAAAATGTGA
W303-Ade2-1 AAAAACTAGCTTAAAAATGTGA
K504E-1-1 AAAAACTAGCTTATAAATGTGA
K504E-1-2 AAAAACTAGCTTATAAATGTGA
K504E-1-3 AAAAACTAGCTTTAAAATGTGA
K504E-8-1 AAAAACTAGCTGAAAAATGTGA
K504E-8-2 AAAAACTAGCTGAAAAATGTGA
K504E-11-1 AAAAACTAGCTGAAAAATGTGA
K504E-11-2 AAAAACTAGCTTATAAATGTGA
K504E-11-3 AAAAACTAGCTTTAAAATGTGA

F

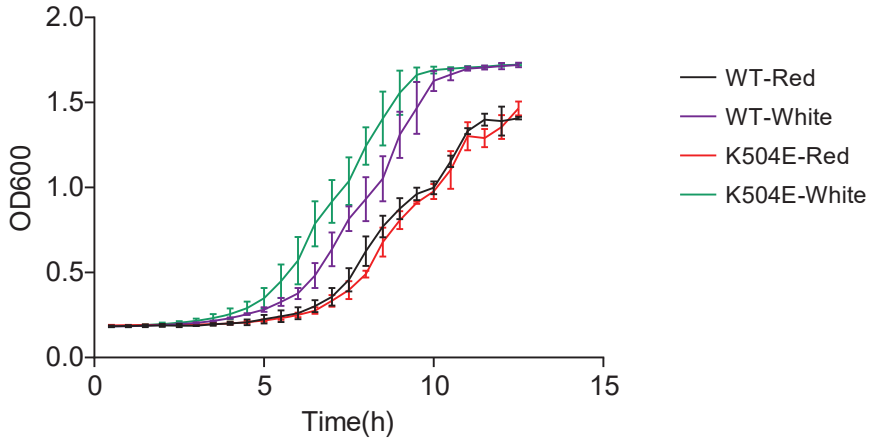
2.0
1.5
1.0
0.5
0.0
OD600
0
5
10
15
Time(h)
WT-Red
WT-White
K504E-Red
K504E-White

G

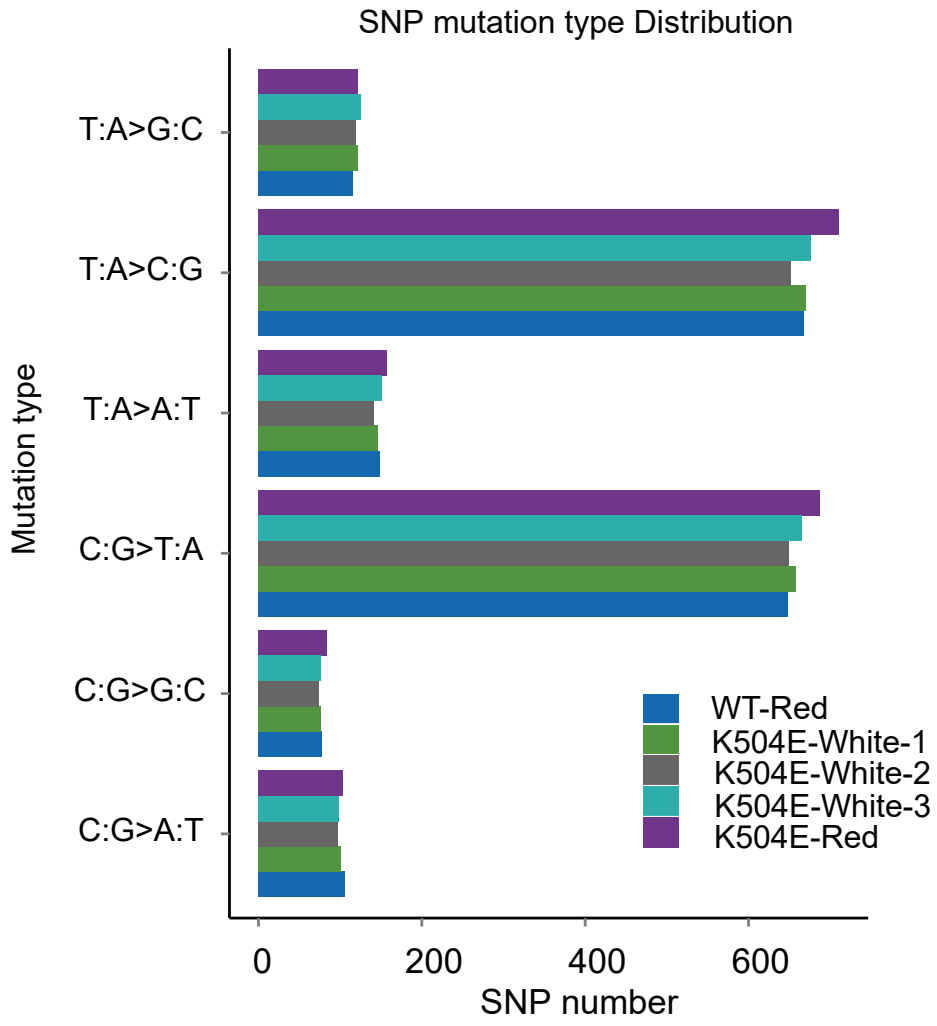
SNP mutation type Distribution
Mutation type
T:A>G:C
T:A>C:G
T:A>A:T
C:G>T:A
C:G>G:C
C:G>A:T
0
200
400
600
SNP number
WT-Red
K504E-White-1
K504E-White-2
K504E-White-3
K504E-Red

Figure S7

A

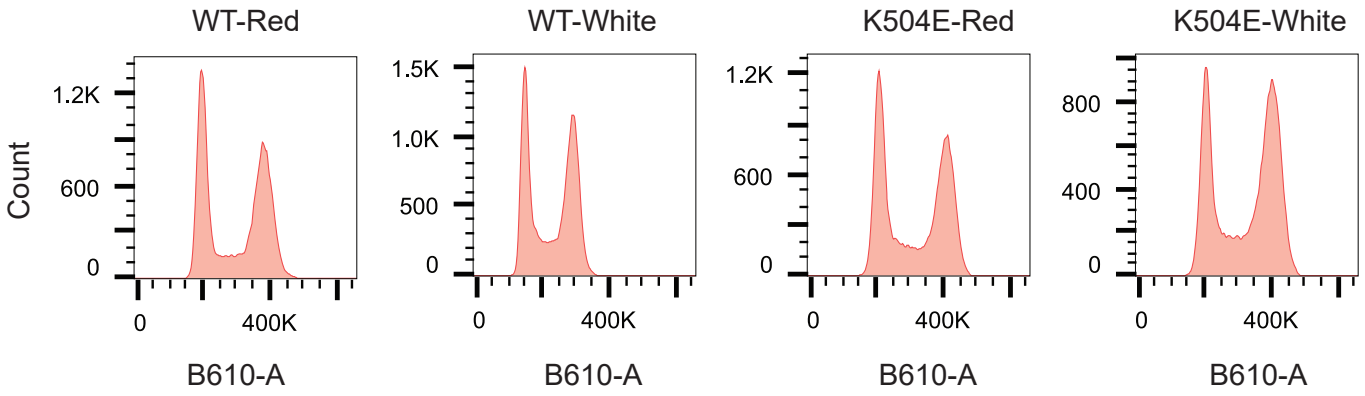

B

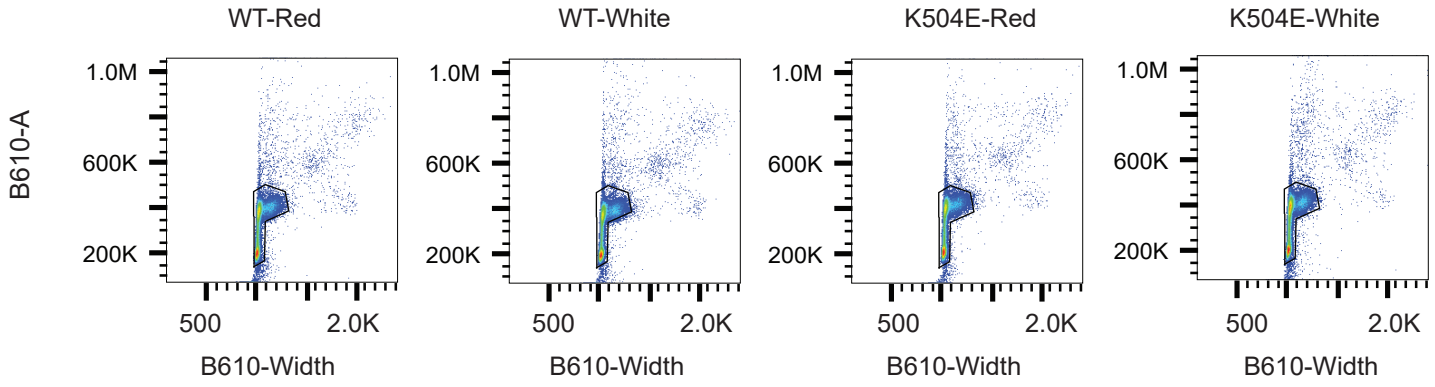

C

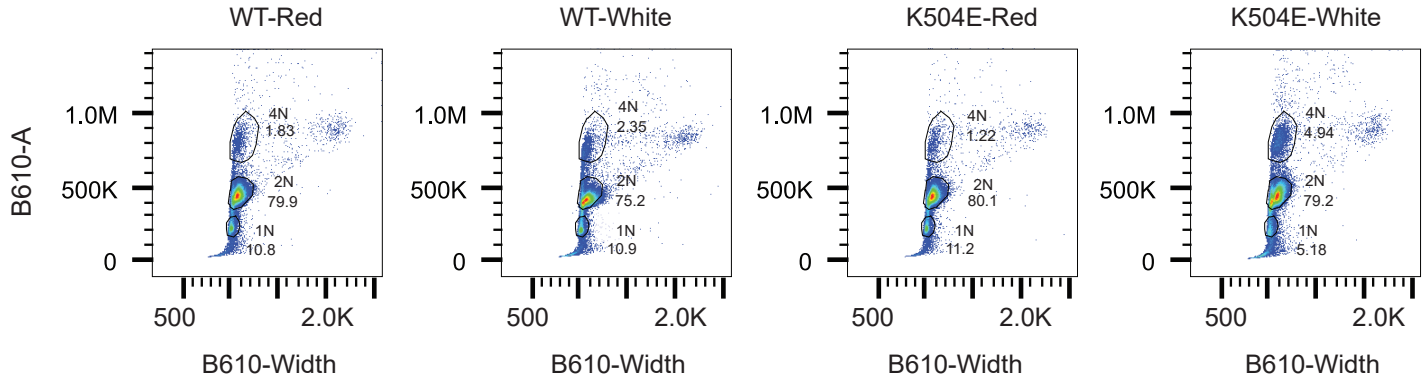

Figure S8

A

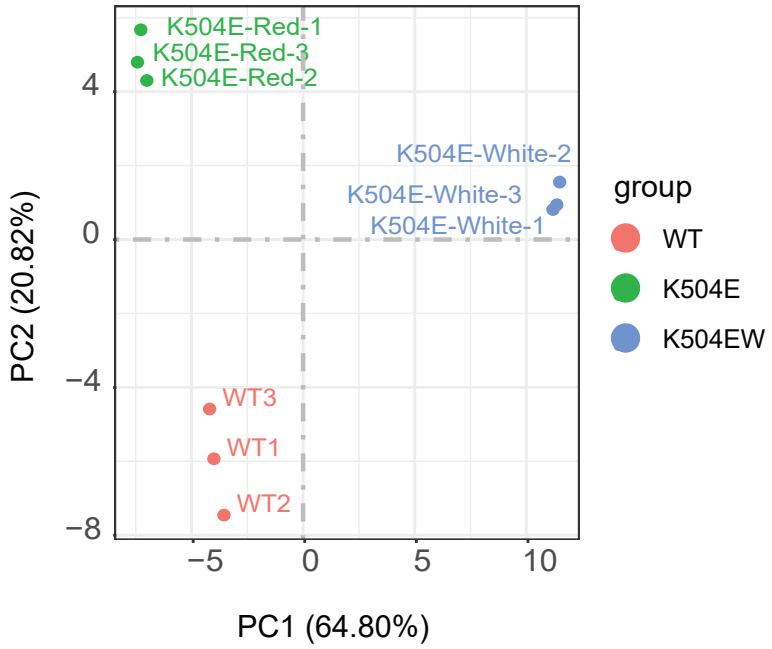

B

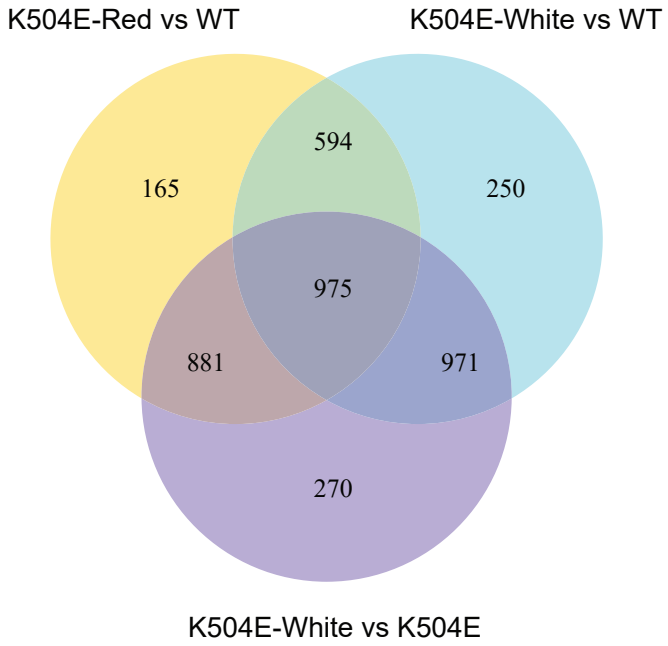

C

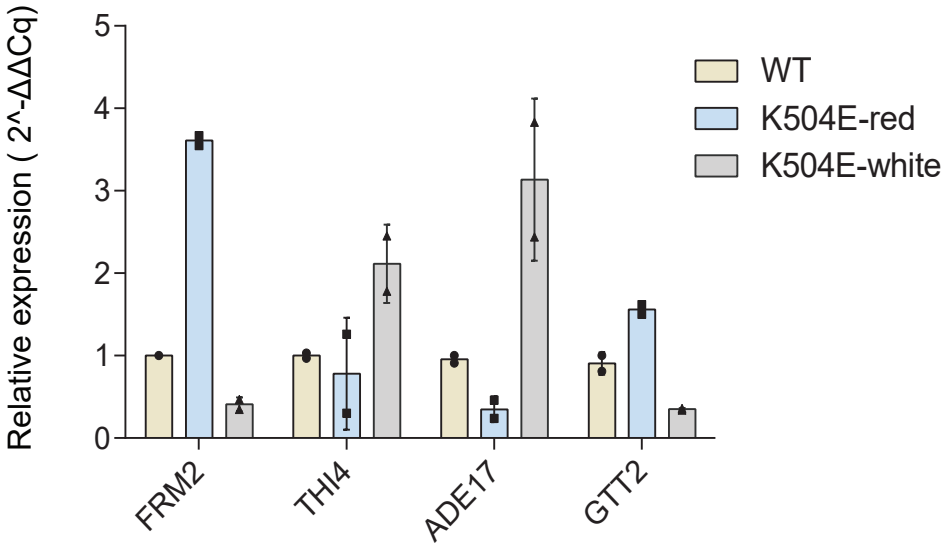

D

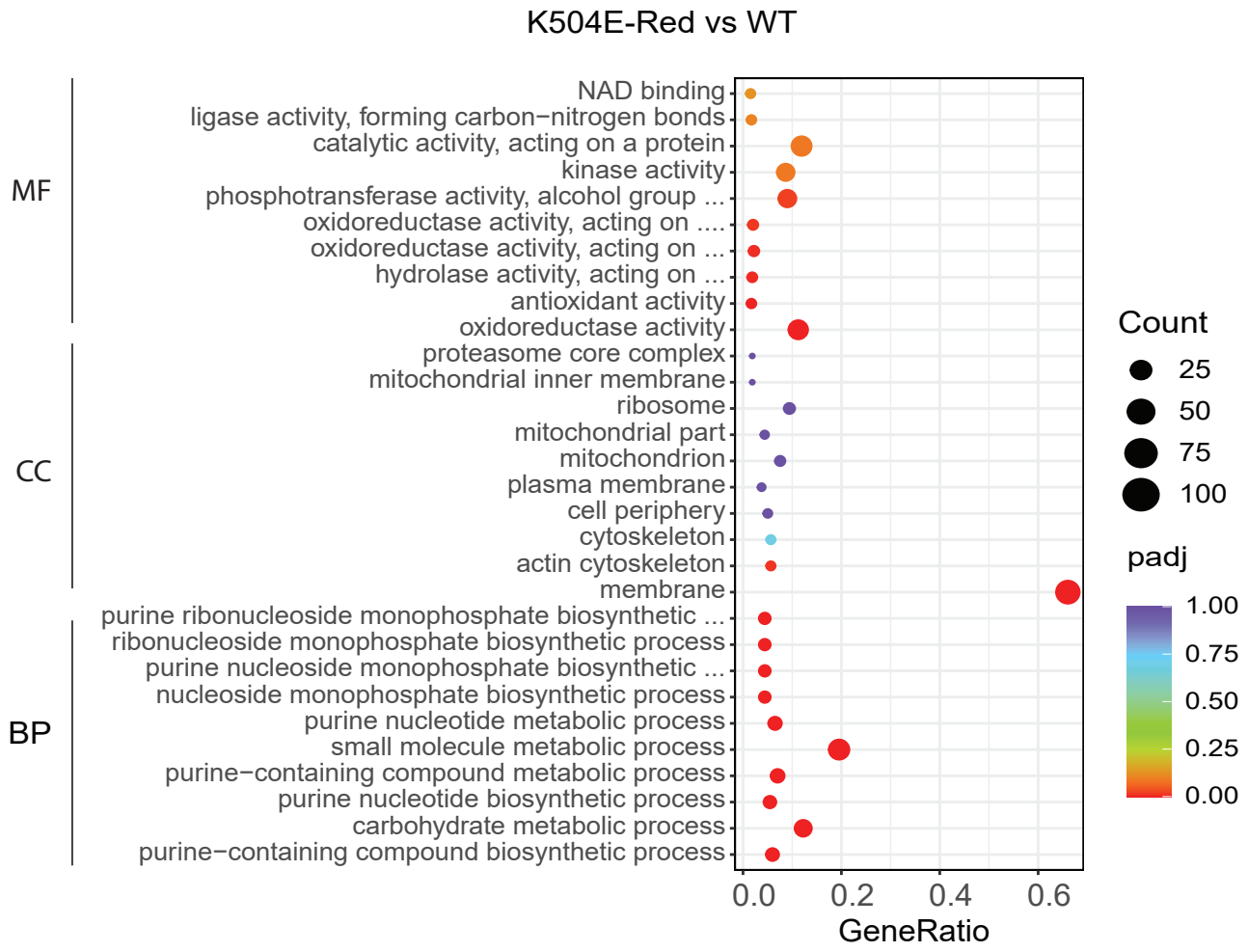
K504E-Red vs WT
MF
CC
BP
NAD binding
ligase activity, forming carbon−nitrogen bonds
catalytic activity, acting on a protein
kinase activity
phosphotransferase activity, alcohol group ...
oxidoreductase activity, acting on ....
oxidoreductase activity, acting on ...
hydrolase activity, acting on ...
antioxidant activity
oxidoreductase activity
proteasome core complex
mitochondrial inner membrane
ribosome
mitochondrial part
mitochondrion
plasma membrane
cell periphery
cytoskeleton
actin cytoskeleton
membrane
purine ribonucleoside monophosphate biosynthetic ...
ribonucleoside monophosphate biosynthetic process
purine nucleoside monophosphate biosynthetic ...
nucleoside monophosphate biosynthetic process
purine nucleotide metabolic process
small molecule metabolic process
purine−containing compound metabolic process
purine nucleotide biosynthetic process
carbohydrate metabolic process
purine−containing compound biosynthetic process
0.0
0.2
0.4
0.6
GeneRatio
Count
25
50
75
100
padj
1.00
0.75
0.50
0.25
0.00

E

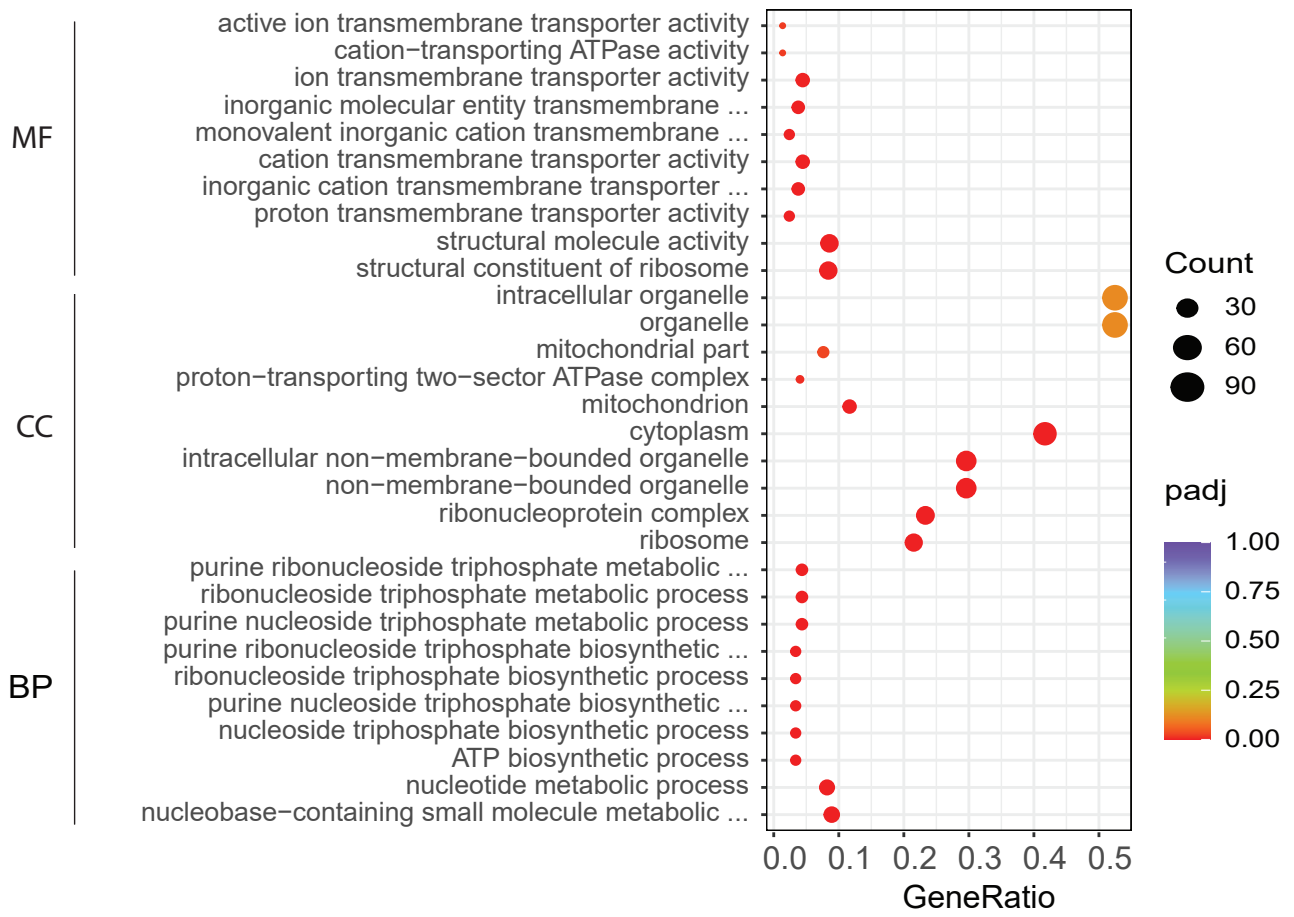
K504E-White vs WT
MF
CC
BP
active ion transmembrane transporter activity
cation−transporting ATPase activity
ion transmembrane transporter activity
inorganic molecular entity transmembrane ...
monovalent inorganic cation transmembrane ...
cation transmembrane transporter activity
inorganic cation transmembrane transporter ...
proton transmembrane transporter activity
structural molecule activity
structural constituent of ribosome
intracellular organelle
organelle
mitochondrial part
proton−transporting two−sector ATPase complex
mitochondrion
cytoplasm
intracellular non−membrane−bounded organelle
non−membrane−bounded organelle
ribonucleoprotein complex
ribosome
purine ribonucleoside triphosphate metabolic ...
ribonucleoside triphosphate metabolic process
purine nucleoside triphosphate metabolic process
purine ribonucleoside triphosphate biosynthetic ...
ribonucleoside triphosphate biosynthetic process
purine nucleoside triphosphate biosynthetic ...
nucleoside triphosphate biosynthetic process
ATP biosynthetic process
nucleotide metabolic process
nucleobase−containing small molecule metabolic ...
0.0
0.1
0.2
0.3
0.4
0.5
GeneRatio
Count
30
60
90
padj
1.00
0.75
0.50
0.25
0.00

Figure S9

```
                                α8          η6          TT      β14
S.                                                                                  .
S.    488  ....SASIDPSRTRMSKMARKDPTIEFCQLGLD.TFETKYITMFGMLVSCSFDK.PAFIS
K.    521  .....................KFPLVRVSNIV..PSASSRYYTVIGLAVTVKYTG.GKTLV
Z.    436  ...................RTRDQLIWFKDLKKQ...DEHYVRMIALLVSSDPKQKGKFAS
E.    510  .....................NALSIDQLSA....TTSSATIFAMLICARVDPGSKVHH
N.    395  ....SNRYDFNSINFIDESTRDQVIQFKDMIIEEENTAKFYIVFGYLLACSTDN.SNYAN
V.    432  KNNNNGKYKSKIKDDMAWNDKDELIKFEDLRVP.INEKIFFKTVGMLISCSFTH.PSFVS

          β15                                   β16         α9          α10
S.                                  TT
S.    542  FVFSDFTKND.IVQNYLYDRYLIDYENKLELNEGFKAIMYKNQFETFDSKLRKIFNNGLR
K.    558  LSFTDFTANPK..VNYGYDSFLGSFQERIPENEHVHALIYLNRVESLNEKLQSIIKMGLM
Z.    475  VIFTDFTKNS.VRQYPLFDKFVVHYEKKLDEDEGIRTLMYLDRYREFGKKIQNVYNKTLD
E.    544  FSFTDFTENLL..ISCKLDPYLNDYCNRLKATECIYVKSYPEYIHNLDAYTLRHYNRRLV
N.    450  FVFTDFTTNRKYEQKYTFDRYINDYNTKLDHDQSFRVISYYNHFNEFNMKVKAKYGKDLN
V.    490  LVFTDFTYNS.IPQKYLFDRFLIDYDNKLELDEGYRVIMYHNQFEEFDEEVKKVYGYSTR

                                η7          β17         TT      β18         η8  α11
S.                                                                                  .
S.    601  DLQNG....RDENLSQYGIVCKMNIKVKMYNGKLNAIVRECEPVPHSQISSIASPSQCEH
K.    616  ECADK....GNSNITHRSIIFKFTVKCQLFQGKLNTVILDADPITPTTPVTT...EEYKL
Z.    534  QTYAP....DTINHSASRIVCVLTLKTKMYRGSLNAVAYGYEPIHAGMTLTL...EERRH
E.    602  DCHNG....RDTNLTNFGMVFRLKLDVKSYQQRINGIIREAVLITGDTRFTG...DEERL
N.    510  AMVNENSQIADKNVSKYGILCRIVMKCKLYQSVLNLVERDIELLDNLHELSIGE...KPY
V.    549  EMIKH....GTENISGIGIICKLSIKGSLYNDKLHLIARKAKILTNSTVRTA...EEDIL

          α12         α13     α14     β19     TT      β20
S.                                                                  .
S.    657  LRLFYQRAFKRIGESAISRYFEEYRRFFPIHRNGSHLAKLRFDEVKHEPKKSPTT.....
K.    669  LKPLRNKIFKRMPSEVIQLYTLTMSRFLPISKNRMSEN....PQLLQEQAFYDSAGSSED
Z.    587  LFQLYQKAIDTR................NVHLLGDRIS.......................
E.    655  LEAFYNRAFQRIENKCFFHNYKRYKVCFPINSLGERNSRLPVPSLLAHTLTL.PA.....
N.    567  IKELFNKTE.............PYLTASPTLNVNGDIASSK.............TT.....
V.    602  INSLFKKSFHRISNSAIMFQFDKFSHCFSITKSNGQIALVTGSELGHDNNNDNHS.....
```

Figure S10

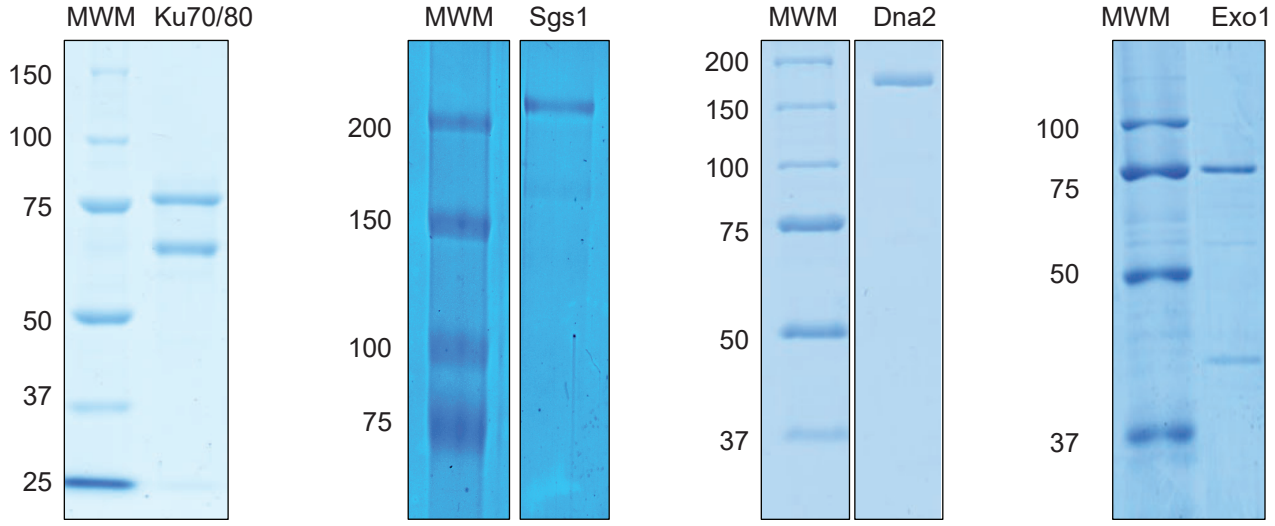

Figure S11

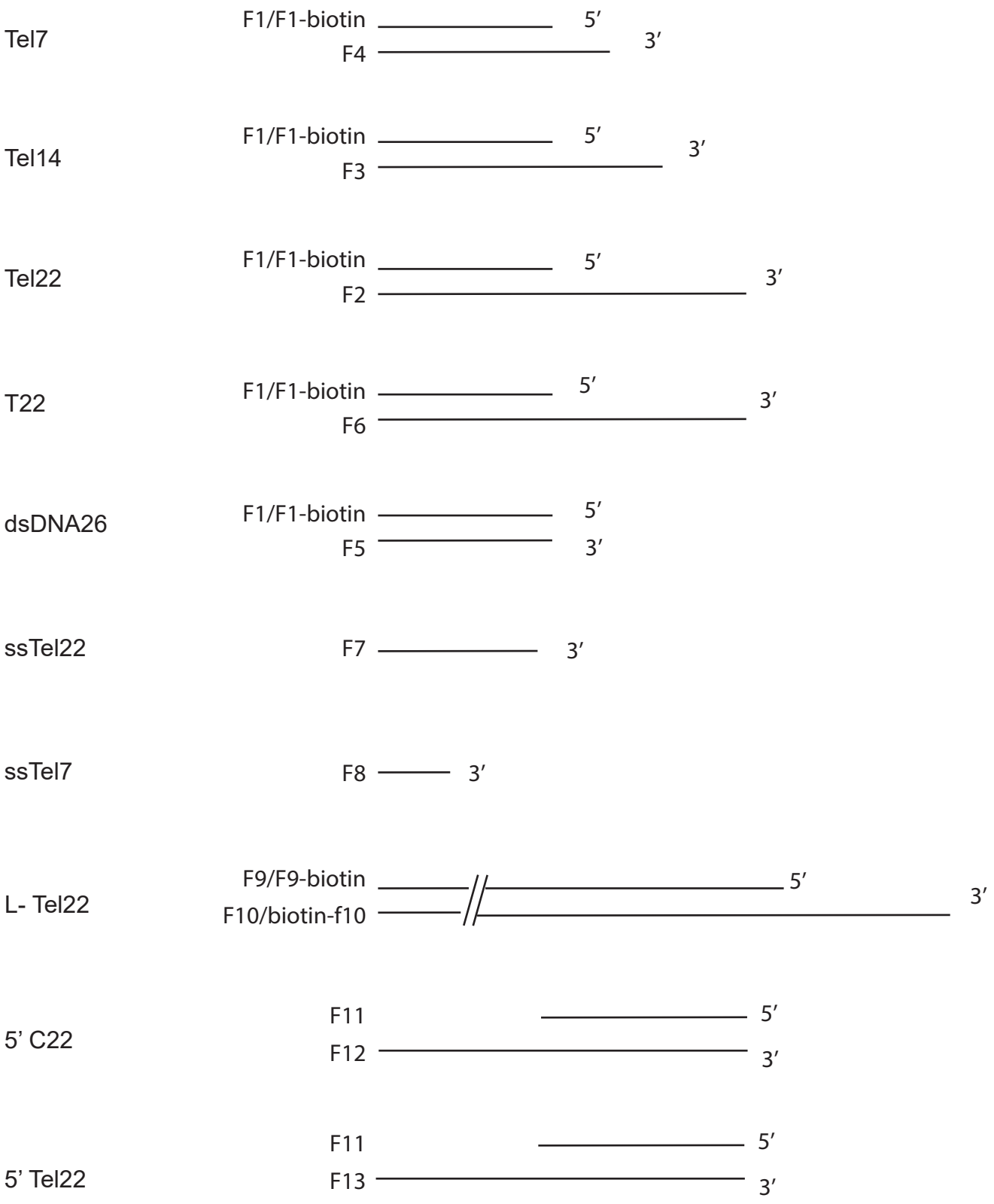
Tel7
F1/F1-biotin
F4
5′
3′
Tel14
F1/F1-biotin
F3
5′
3′
Tel22
F1/F1-biotin
F2
5′
3′
T22
F1/F1-biotin
F6
5′
3′
dsDNA26
F1/F1-biotin
F5
5′
3′
ssTel22
F7
3′
ssTel7
F8
3′
L- Tel22
F9/F9-biotin
F10/biotin-f10
5′
3′
5’ C22
F11
F12
5′
3′
5’ Tel22
F11
F13
5′
3′

Table S1

Substrate	Sequence
F1	ACACCCACTCTACGTCTTATCATTAT
F1-ibiotin	ACACCCACTCTACGTCTTATCAT/iBiodT/AT
F2	ATAATGATAAGACGTAGAGTGGGTG T GTGTGTGGGGTGGTGTGTGTGG
F3	ATAATGATAAGACGTAGAGTGGGTGTGTGTGTGGGGTGGT
F4	ATAATGATAAGACGTAGAGTGGGTGTGTGTGTG
F5	ATAATGATAAGACGTAGAGTGGGTGT
F6	ATAATGATAAGACGTAGAGTGGGTGTAACTGTAGCTCTTCGTTCCGTC
F7	TGTGGGTGTGGTGTGGGTGTGG
F8	GTGTGTG
F9	ACACCCACATAAGAAAGCTTAATCTTGTCGTCATCCTTGTAGTCTACTGTTGTCTGAA
F9-biotin	ACACCCACATAAGAAAGCTTAATCTTGTCGTCATCCTTGTAGTCTACTGTTGTCTGAA/3'Bio/
F10	TTCAGACAACAGTAGACTACAAGGATGACGACAAGATTAAGCTTTCTTATGTGGGTGTGTGTGTGGGGTGGTGTGTGTGG
biotin-F10	/5Biosg/TTCAGACAACAGTAGACTACAAGGATGACGACAAGATTAAGCTTTCTTATGTGGGTGTGTGTGTGGGGTGGTGTGTGTGG
F11	TCTACGTCTTATCATTATACACCCAC
F12	GTGTGTGGGGTGGTGTGTGTGGGTGGGTGTATAATGATAAGACGTAGA
F13	CCACACCCACACCACACCCACAGTGGGTGTATAATGATAAGACGTAGA

Table S2

Strain	Genotype
HKY3415-11 (WT)	*MATa SRS2-TAP-TRP1, leu2-3, 112 his3-11, 15 ade2-1, ura3-1, trp1-1, can1-100, RAD5+*
cdc13-K504E	HKY3415-11 *cdc13*-K504E
ku80Δ	HKY3415-11 *ku80::KanMX*
cdc13-K504E/ *ku80Δ*	HKY3415-11 *cdc13-K504E, ku80::KanMX*